ARL-TR-8831 ● Oct 2019

Radar Assimilation over Kwajalein Atoll

by Brian P Reen, Huaqing Cai, and John W Raby

NOTICES

Disclaimers

ARL-TR-8831 ● OCT 2019

Radar Assimilation over Kwajalein Atoll

Brian P Reen, Huaqing Cai, and John W Raby
Computational Information Sciences Directorate,
CCDC Army Research Laboratory

REPORT DOCUMENTATION PAGE	*Form Approved* *OMB No. 0704-0188*

1. REPORT DATE *(DD-MM-YYYY)*	2. REPORT TYPE	3. DATES COVERED (From - To)
October 2019	Technical Report	January 2018–August 2019

4. TITLE AND SUBTITLE
Radar Assimilation over Kwajalein Atoll

5a. CONTRACT NUMBER

5b. GRANT NUMBER

5c. PROGRAM ELEMENT NUMBER

6. AUTHOR(S)
Brian P Reen, Huaqing Cai, and John W Raby

5d. PROJECT NUMBER

5e. TASK NUMBER

5f. WORK UNIT NUMBER

7. PERFORMING ORGANIZATION NAME(S) AND ADDRESS(ES)
CCDC Army Research Laboratory
ATTN: FCDD-RLC-EM
2800 Powder Mill Road
Adelphi, MD 20783-1138

8. PERFORMING ORGANIZATION REPORT NUMBER
ARL-TR-8831

9. SPONSORING/MONITORING AGENCY NAME(S) AND ADDRESS(ES)
CCDC Aviation and Missile Center

10. SPONSOR/MONITOR'S ACRONYM(S)
AvMC

11. SPONSOR/MONITOR'S REPORT NUMBER(S)

12. DISTRIBUTION/AVAILABILITY STATEMENT
Approved for public release; distribution is unlimited.

13. SUPPLEMENTARY NOTES
ORCID IDs: Brian Reen, 0000-0002-2031-4731

14. ABSTRACT
Radar-reflectivity observations from the Kwajalein Atoll were converted into 3-D fields of latent heating temperature tendency terms (LHT) and used to replace the microphysics temperature tendency term in the Weather Research and Forecasting numerical weather prediction model for two cases on the same day. Applying LHT from a series of 15-min radar observations during a preforecast data-assimilation period substantially improved short-term reflectivity forecasts. The benefits last longer for forecasting overall coverage of reflectivity compared to forecasting placement of convection. The length that improvements in placement last vary substantially between the two cases with improvement lasting approximately 3 h for the case with stronger, more widespread convection, and improvement lasting <1 h for the other case. The radar data provide the most benefit when the data-assimilation period is longer, with 6-h assimilation periods usually performing better than 2-h and 1-h assimilation periods. Potential benefits were seen by changing the LHT to zero when the model forecasted reflectivity too high to prevent overstimulation of convection. It was not clear if adding a cooling term to more efficiently suppress erroneous convection was beneficial.

15. SUBJECT TERMS
data assimilation, radar, latent heating, mesoscale modeling, WRF, Weather Research and Forecasting, WRE-N, WREN_RT

16. SECURITY CLASSIFICATION OF:			17. LIMITATION OF ABSTRACT	18. NUMBER OF PAGES	19a. NAME OF RESPONSIBLE PERSON
					Brian P Reen
a. REPORT	b. ABSTRACT	c. THIS PAGE	UU	54	19b. TELEPHONE NUMBER (Include area code)
Unclassified	Unclassified	Unclassified			301-394-3072

Standard Form 298 (Rev. 8/98)
Prescribed by ANSI Std. Z39.18

Contents

List of Figures

Acknowledgments

The US Army Combat Capabilities Development Command (CCDC) Aviation and Missile Center (AvMC) provided funds that supported the research described in this technical report. We thank Shawn Ericson and Mariana Scott (Integration Innovation, Inc.) for their assistance and guidance. We thank Ming Hu (National Oceanic and Atmospheric Administration [NOAA]/Global System Division/Cooperative Institute for Research in Environmental Sciences and the Developmental Testbed Center) for providing very helpful advice and also providing software for converting multiradar multisensor radar data into the format needed by the Gridpoint Statistical Interpolation software; this software was adapted by the CCDC Army Research Laboratory to process archived Kwajalein radar data. We acknowledge Mike Dixon (National Center for Atmospheric Research [NCAR]) for providing assistance in using Radx (part of the Lidar Radar Open Software Environment) to process the radar data.

The Model Evaluation Tools (MET) was used for verification. MET was developed by NCAR through grants from the US Air Force Weather Agency and NOAA. The NCAR Command Language (http://dx.doi.org/10.5065/D6WD3XH5) was used for creating some of the graphics in this report.

1. Introduction

Forecasts of hydrometeors (e.g., snowflakes and raindrops) are important for the testing of high-speed flight systems since they can be damaged by interactions with hydrometeors. Therefore, we investigate improving forecasts of hydrometeors by assimilating radar data into a numerical weather prediction model over the Ronald Reagan Ballistic Missile Defense Test Site on Kwajalein Atoll (Republic of the Marshall Islands).

Weather radar provides meteorological information at much higher spatial and temporal resolution than many other sources of weather observations and thus is an attractive data set to assimilate into numerical weather prediction models. However, there are a variety of methods that can be used to assimilate these data and more than one field is observed by modern weather radars. Therefore, assimilating radar data involves choosing which fields to assimilate and which methods to use to assimilate them.

Reflectivity and radial velocity are two commonly assimilated radar fields. Reflectivity is a measure of the power of the portion of the radar beam that is backscattered to the radar (e.g., Markowski and Richardson 2010), and thus provides information on the objects that caused the backscattering, such as hydrometeors. Radial velocity is the component of the velocity along the radar beam and can be computed in Doppler radars. Dual-polarization radars provide additional fields that can assist in characterizing the hydrometeors present. In this study we focus on assimilation of reflectivity since it seemed the radar field most likely to lead to improvements in forecasts of hydrometeors.

Some methods available to assimilate reflectivity include 3-dimensional variational data assimilation (3DVAR), 4-dimensional variational data assimilation (4DVAR), and the ensemble Kalman filter (EnKF). The process of assimilating reflectivity is made less direct due to reflectivity being a diagnostic variable rather than a prognostic variable in numerical weather prediction models such as the Advanced Research version of the Weather Research and Forecasting model (WRF-ARW; Skamarock et al. 2008).

3DVAR builds an analysis that minimizes a cost function that includes terms measuring the difference between the analysis and the background (first-guess) field and the difference between the analysis and the observations. It includes a matrix of the covariance of the background errors and a matrix of the covariance of the observation errors; these allow the analysis to account for errors in the background and observations and how the errors relate spatially and among variables. However, in practice these may be simplified; for example, the observation error between any two observations might be assumed to not be related. This technique will perform best if one has a good estimate of the background error covariance; however, this can be difficult to obtain. Additionally, the background error covariance in pure 3DVAR is not flow dependent, and so does not account for temporal variations. In applying 3DVAR to radar-reflectivity observations, one must determine how the radar-reflectivity observations relate to prognostic fields in the model such as hydrometeors. Determining adequate background error covariances may be especially difficult for assimilating reflectivity given that reflectivity and hydrometeors are highly heterogeneous with large areas where they are effectively nonexistent; this may require a different variable be used to calculate background error covariances (e.g., Xiao and Sun 2007). One example of a system that can assimilate radar reflectivity data using 3DVAR is WRF Data Assimilation (WRFDA; Barker et al. 2012) with methods used in WRFDA for 3DVAR assimilation of radar reflectivity described in the user's guide (http://www2.mmm.ucar.edu/wrf/users/wrfda/Docs/user_guide_V3.9.1/users_guide_chap6.htm#precipitation) and various publications (e.g., Xiao and Sun 2007; Wang et al. 2013).

4DVAR builds on 3DVAR by incorporating the time dimension through integrating some representation of the numerical weather prediction model forward and backward. This allows an analysis of the initial conditions to be created based on a cost function that includes the numerical weather prediction model as a dynamical constraint. This method is more computationally intensive than 3DVAR and requires an adjoint model to integrate backward. Carlin et al. (2017) indicate that the application of 4DVAR methods to radar assimilation have been limited and cite nonlinearities in microphysics and challenges in creating and updating adjoint models as contributing to this.

EnKF uses an ensemble of simulations to better capture the background error covariance specific to the current conditions. However, running multiple ensemble members necessarily increases the computational requirements; also, many ensemble members would be necessary to adequately represent the background error covariance and so techniques must be applied to account for this. An example of radar assimilation via EnKF is the National Severe Storms Laboratory Experimental Warn-on-Forecast system for ensembles (Lawson et al. 2018).

Other techniques have also been used to apply information gained from radar reflectivity observations to the numerical weather prediction model. One example is the cloud analysis in the variational Local Analysis and Prediction System (vLAPS; Jiang et al. 2015). Although vLAPS uses variational assimilation for some variables, the cloud analysis remains nonvariational—a technique first described in Albers et al. (1996). As described in Reen et al. (2017), radar observations are combined with other data sources to create a cloud analysis, which is then used to determine a 3-D hydrometeor field and a vertical velocity that influences the 3-D wind field. Carlin et al. (2017) notes various other techniques, but latent heat techniques are of particular interest in this report since that technique was applied for the research reported herein.

Using radar reflectivity data to solely specify hydrometeors in a numerical weather prediction (NWP) model may not be effective, because without dynamics to support the hydrometeors they will tend to evaporate or sublimate. In other words, if you simply insert rain into the model but the vertical motion fields in the model do not even support clouds, the rain will likely evaporate and cool the column and thus the observed radar reflectivities on which the assimilation was based will not be seen in the model-predicted reflectivities.

The assimilation of weather radar information through the addition of latent heating terms has been applied in a variety of models. For example, Wang and Warner (1988) used a precipitation estimate based on radar and gauge data to construct a 3-D latent heat field that was applied for either 1 or 2 h to 30-km horizontal grid spacing simulations of the Pennsylvania State University–National Center for Atmospheric Research (NCAR) mesoscale model Version 4. Jones and Macpherson (1997) described the latent-heating-nudging methodology implemented into the then-operational 17-km horizontal grid-spacing mesoscale version of the United Kingdom Met Office's (UKMET) Unified Model. (They also note the use of nudging as the methodology they use for assimilation of other observations). The heating calculated by the model to be due to cloud processes was scaled by the ratio of observed rain rate to modeled rain rate, where the observed rain rate was a 3-h analysis combining radar and gauge data; these data were temporally interpolated and generally applied for a 6-h period. One challenging aspect of this methodology is that in cases where observations indicate rainfall but the model indicates no (or much less) rainfall, scaling the latent heating profile is problematic and so a nearby latent-heating profile must be found in the model where more precipitation is occurring. UKMET no longer uses nudging as their primary assimilation technique; they still use latent heat nudging, although now based on radar reflectivity (Barker 2019).

Stephan et al. (2008) modified the scheme of Jones and Macpherson (1997) and applied it to the Deutscher Wetterdienst's (Germany's national weather service) operational 2.8-km horizontal grid spacing COSMO-DE model (high resolution version of the Consortium for Small Scale Modelling model). One of the modifications they applied included changing the quantity used to compare against observed precipitation to be the vertically integrated precipitation flux rather than the modeled precipitation rate. This is an attempt to account for the fact the latent heat release associated with precipitation occurs before the precipitation reaches the ground. They also prevented the use of observation-derived negative heating rates, and used much finer temporal resolution precipitation observations (every 5 min), along with other modifications.

As of Benjamin et al. (2016), the 13-km WRF-ARW-based Rapid Refresh (RAP) model used 3-D radar reflectivity data to calculate a 3-D latent heating rate that was applied during a 20-min forward digital filter initialization (DFI) step. Lightning data also were used to determine the latent heating, which was then constrained by satellite data. Additionally, satellite and surface observations were used to adjust the hydrometeor fields (and other fields). The 3-km WRF-ARW-based High-Resolution Rapid Refresh (HRRR) model also uses 3-D radar reflectivity data to calculate a 3-D latent heating rate. However, this is done without DFI during a 1-h preforecast time period using a series of 15-min radar reflectivity fields (Alexander et al. 2017). The use of 3-D reflectivity rather than precipitation data removes the difficulty of determining how to apply a 2-D field in 3-D. It also makes it easier to apply the latent heating at the proper time since the latent heating is based on the 3-D reflectivity itself rather than the precipitation that falls associated with that reflectivity (over whatever time period the precipitation is allowed to accumulate before being used to compute latent heating). In this study, we apply the technique used in the 3-km HRRR to 1-km WRF-ARW simulations over Kwajalein Atoll.

Section 2 describes the WRF-ARW and its configuration for this study and Section 3 describes the case investigated. The methodology is described in Section 4, the experimental design in Section 5, and the results in Section 6. Section 7 provides the summary, conclusions, and future work.

2. Model Description and Configuration

The WRF-ARW (often called simply WRF) V3.9.1.1 (Skamarock et al. 2008) is applied in this research. The Weather Running Estimate–Nowcast Realtime system (WREN_RT; Reen and Dawson 2018) was used to assist in the preparation of input data for the WRF simulations. While WREN_RT can carry out both the preparation of input data and the running of WRF, the capability to assimilate radar-reflectivity data is not yet included in WREN_RT and thus WREN_RT could not carry out the entire process for this study.

The model was configured with 9-, 3-, and 1-km horizontal grid-spacing nested domains centered over the region of the Kwajalein Atoll (Fig. 1), which is in the Marshall Islands in the Pacific Ocean. The 9-km domain contains 151 × 151 gridpoints, the 3-km 193 × 163, and the 1-km 223 × 211, and all domains contain 56 vertical levels.

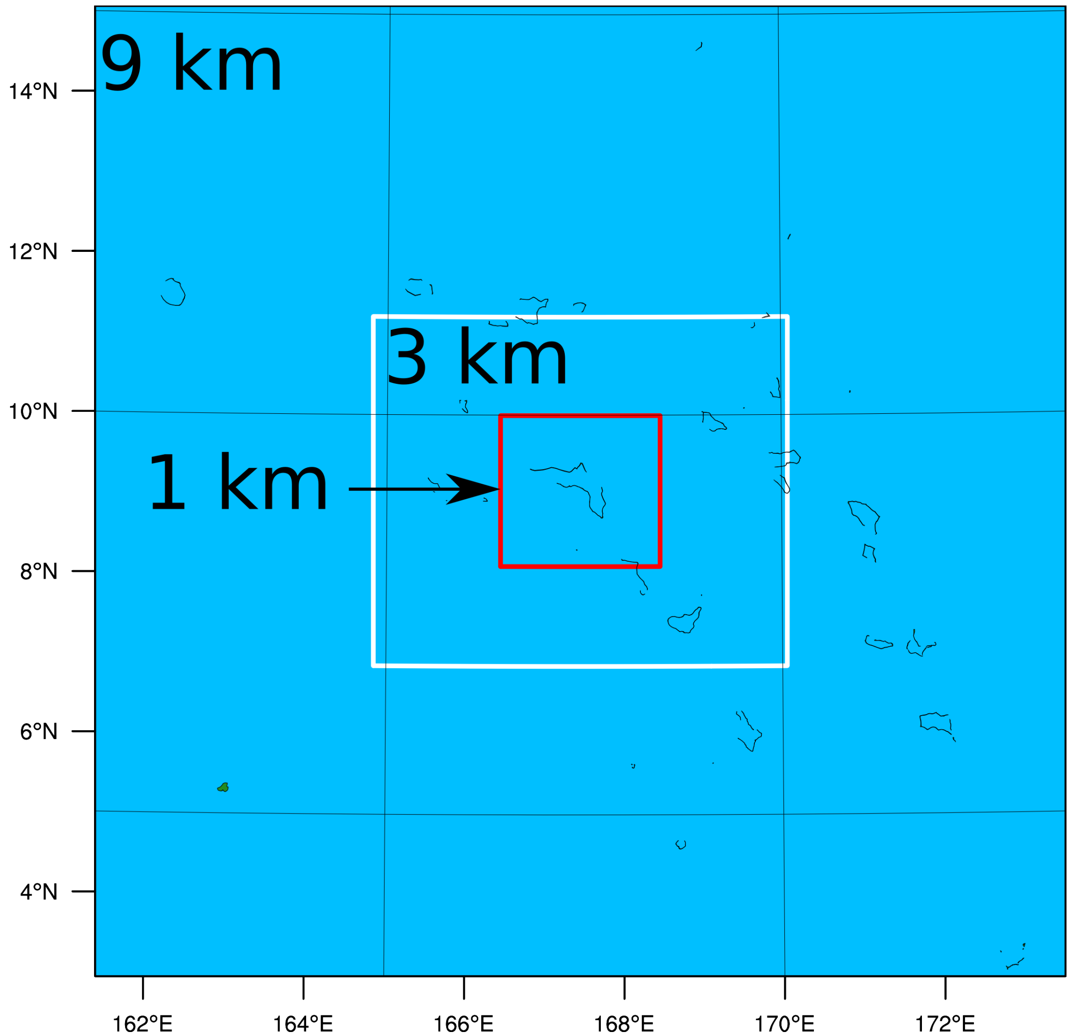

Fig. 1 Horizontal extent of the WRF-ARW 9-, 3-, and 1-km horizontal grid-spacing domains, which are centered over the region of the Kwajalein Atoll

The first guess for initial conditions is supplied by 0.50° resolution Global Forecast System (GFS) data. However, the sea surface temperature is specified via the National Centers for Environmental Prediction (NCEP) 1/12° horizontal grid-spacing Real-Time Global Sea Surface Temperature (Gemmill et al. 2007).

The GFS-derived first-guess fields used to specify the WRF-ARW initial conditions are enhanced by applying a multiscan Cressman-based analysis via the Obsgrid program (NCAR 2017). The observations included in the analysis are obtained from the Meteorological Assimilation Data Ingest System (MADIS; https://madis.ncep.noaa.gov/) database. Specifically, any available MADIS observations from its Aircraft Communications Addressing and Reporting System, rawinsonde, and satellite wind categories are ingested. Surface observations are avoided because early simulations suggested that assimilation of surface observations could be problematic; the 1-km domain contains a single observation and thus the observation can serve to create a warm bubble that erroneously causes convection early in the simulation over Kwajalein Atoll. The multiscan Cressman analysis is carried out separately on each model domain, but an area larger than the domain is used to carry out the analysis to ensure that observations outside the domain, and yet within the radius of influence, can be included.

The parameterizations chosen closely match the WRF-ARW tropical parameterization suite (http://www2.mmm.ucar.edu/wrf/users/wrfv3.9/tropical_suite.html). As in the tropical physics suite, the following physics parameterizations are used: YSU (Yonsei University in Seoul, South Korea) planetary boundary layer (PBL) parameterization (Hong et al. 2006), WSM6 (WRF single-moment 6-class) microphysics (Hong and Lim 2006), new Tiedtke cumulus parameterization (Zhang and Wang 2017), the Noah land-surface model (Tewari et al. 2004), and the RRTMG (rapid radiative transfer model for general circulation models) shortwave and longwave radiation schemes (Iacono et al. 2008). However, the revised Pennsylvania State University–NCAR mesoscale model Version 5 (MM5) surface-layer scheme (Jimenez et al. 2012) is used instead of the standard MM5 surface-layer scheme included in the tropical suite. Additionally, the cumulus parameterization is only applied on the 9-km domain in this study since deep convection should be partially resolved on the 3- and 1-km domains.

3. Case Description

Two forecast starting times on the same day, 0100 and 0600 coordinated universal time (UTC) on 10 Sep 2016, were examined as two cases (referred to as Case A and Case B). Note that local time (Marshall Islands Time [MHT]) is 12 h ahead of UTC and thus the forecast starting times are 1300 and 1800 MHT. For many experiments, the model was run before the forecast starting time to spin up the model and assimilate the radar-reflectivity data, so times before the forecast start time are also of interest. Plots of the 1-km above ground level (AGL) reflectivity from the Kwajalein radar are shown in Fig. 2 for 1900 UTC on 9 Sep through 1200 UTC on 10 Sep 2016. The radar data were interpolated to the 1-km numerical weather-prediction domain used in this study to facilitate comparison with model forecast reflectivity. While returns are visible throughout the period shown, how much of the domain is covered and the size of the structures seen in the reflectivity vary widely. For example, at 1900 UTC there are only a few small reflectivity structures, whereas by 0100 UTC there are much larger-scale structures visible in the reflectivity.

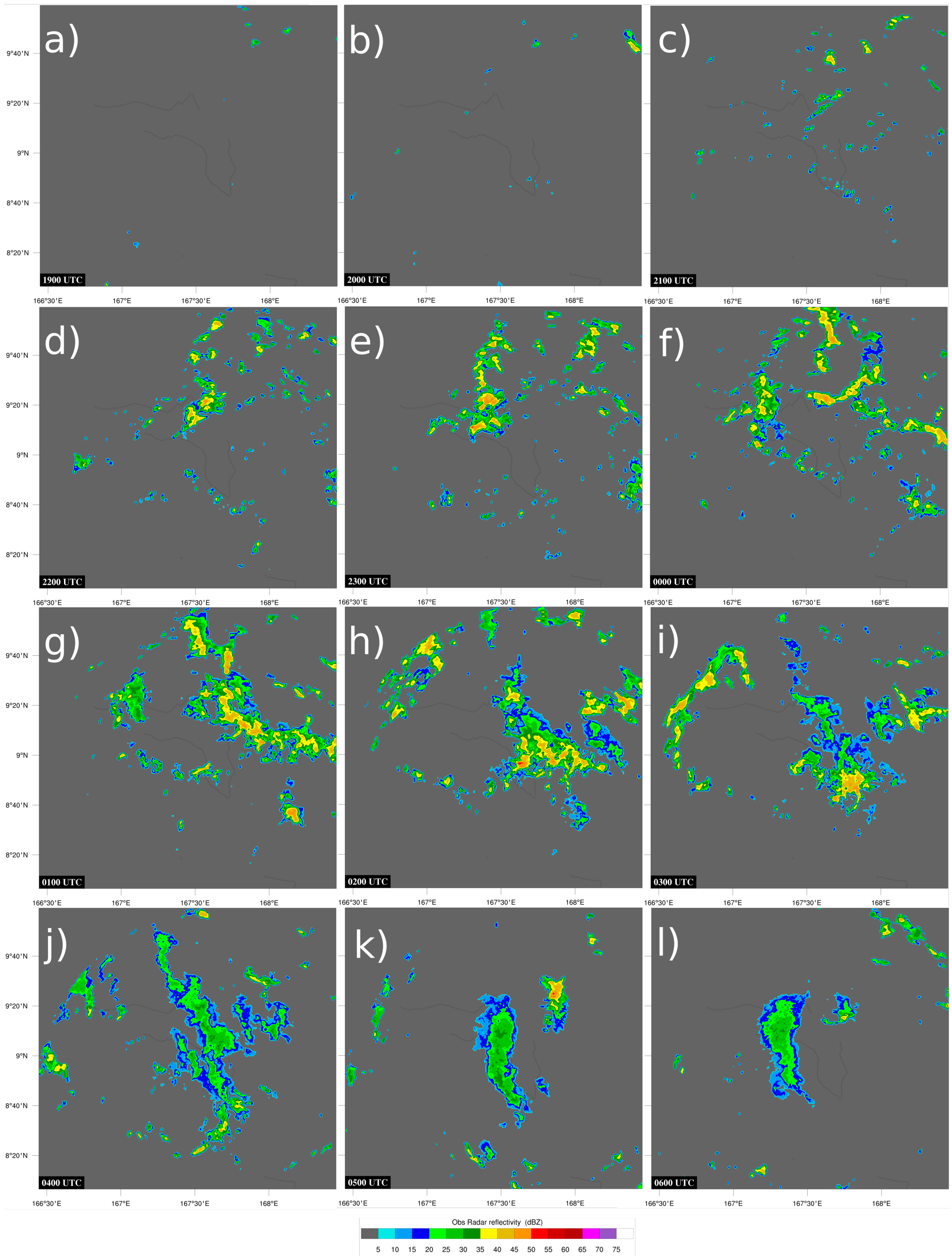

Fig. 2 Radar reflectivity at 1 km AGL observed by the radar at Kwajalein Atoll (the thin black line shows the location of the atoll) and shown here at hourly intervals starting at 1900 UTC on 9 Sep (a) through 1200 UTC on 10 Sep 2016 (x); reflectivity is interpolated to the 1-km NWP model domain; the radar observation closest to each hour is shown and it is labeled as being at that hour although the actual observation was not necessarily exactly at the hour

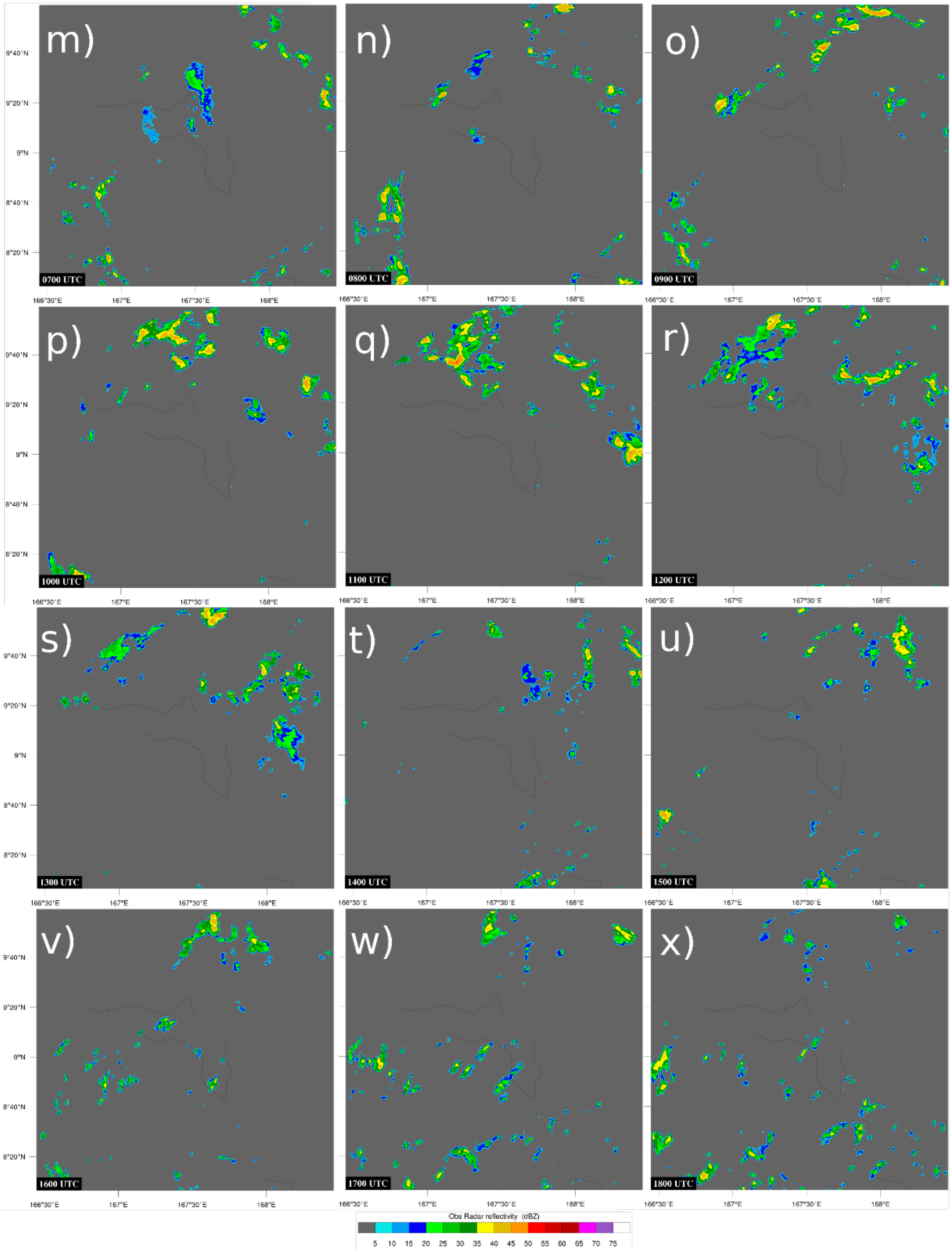

Fig. 2 Radar reflectivity at 1 km AGL observed by the radar at Kwajalein Atoll (the thin black line shows the location of the atoll) and shown here at hourly intervals starting at 1900 UTC on 9 Sep (a) through 1200 UTC on 10 Sep 2016 (x); reflectivity is interpolated to the 1-km NWP model domain; the radar observation closest to each hour is shown and it is labeled as being at that hour although the actual observation was not necessarily exactly at the hour (continued)

4. Methodology

Data from the Kwajalein Atoll weather radar were obtained and converted to the format required for ingestion by the Gridpoint Statistical Interpolation (GSI; Shao et al. 2016) software. GSI then created a series of 3-D fields of radar-derived latent heating temperature tendency terms (LHT) for ingestion by WRF-ARW. These fields were used by WRF-ARW during a preforecast data-assimilation period and the results were evaluated using two metrics.

4.1 Preparing Radar Data for GSI

Radar data come in various formats depending on the kind of radar system that collects the data as well as the radar manufacturer. The radar on Kwajalein Atoll is an S-band Doppler radar similar to the WSR-88D radar network that covers the continental United States (CONUS). We obtained the Kwajalein radar data, which has been preprocessed and quality controlled by NASA, in a format called Universal Format (UF). Unfortunately, GSI requires all of its input data in BUFR (the Binary Universal Form for the Representation of meteorological data), which is a binary format maintained by the World Meteorological Organization to facilitate data sharing among its member nations. A thorough survey of radar-processing software was conducted and no off-the-shelf software tool was available to convert UF to BUFR format. We thus needed to develop a new software tool to perform the radar-data format conversion so assimilating radar data from Kwajalein using GSI would be possible.

NCAR developed a software package called RADX, which is open source and readily available as a community resource. RADX can read radar data in UF format, perform interpolation of radar data from radar coordinates onto 3-D Cartesian coordinates, and write out the gridded radar data in NetCDF format. Complementary to this, the software package "process_mosaic" provided by Dr Ming Hu from the National Oceanic and Atmospheric Administration/Global System Division (NOAA/GSD) can read a 3-D Cartesian grid in NetCDF format and then convert it to BUFR format. The process_mosaic software is designed to process the National Severe Storms Laboratory's multiradar multisensor (MRMS; https://mrms.nssl.noaa.gov/; Zhang et al. 2005) product that is a mosaic of radar data available over the continental United States. Therefore, to achieve our goal of converting UF format to BUFR, we modified Dr Hu's code so it can ingest the NetCDF data created by RADX and put them in the proper arrays needed for converting them into BUFR format; this variant of process_mosaic is known as process_radx. The software tool encompassing RADX and process_radx, which is called radx2bufr, was thus developed, tested, and used in this project. Its flowchart is shown in Fig. 3, which summarizes the processes necessary to accomplish the data-format conversion required by GSI. As illustrated in Fig. 3, there are two major components of the software tool: one is RADX developed by NCAR, the other is process_radx developed by the CCDC Army Research Laboratory based on Dr Hu's code, and these work together to fulfill the conversion of original radar data in UF format to 3-D gridded radar data in BUFR format.

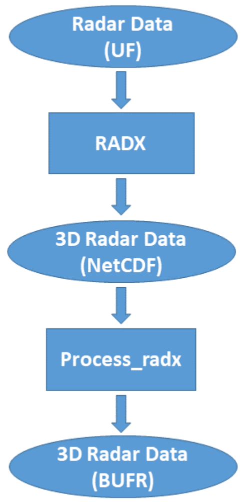

Fig. 3 Processes employed by the radx2bufr software tool to convert original radar-reflectivity data from UF format to 3-D gridded radar-reflectivity data in BUFR format

The details of the radx2bufr software tool are not relevant for this report and are therefore not included here (the tool will be documented in a separate report: Cai et al. [forthcoming]). However, note that 1) this tool only deals with radar-reflectivity data, 2) the 3-D gridded radar-reflectivity data produced by the tool has the same map projection and domain as the WRF model, and 3) some special considerations have to be made within the software so that at each grid point, the BUFR data contains only one of the three kinds of possible output values (i.e., a regular radar-reflectivity value, a flag representing no storms [–63], or a flag representing missing data [–64]). The ability to distinguish these three kinds of data is crucial for radar data assimilation using GSI, as will be demonstrated later in this report.

4.2 Preparing WRF Initial Condition Files for GSI

Before executing GSI, the user must create WRF initial condition files—named *wrfinput_dXX*, where XX is the 1-based domain number (e.g., *wrfinput_d01*)—into which GSI will place the radar-derived LHT. GSI will need a separate WRF initial conditions file for each time it creates LHT. For this investigation we are solely using GSI to create LHT (and not using the analyses of other fields created by GSI). It appears the only way in which the WRF initial condition file affects the LHT is that it uses the fields in the WRF input file to find an atmospheric boundary layer (ABL, also known as the PBL) depth to use in determining how deep of a layer to exclude the LHT from near the surface. Due to the impact of the GSI-diagnosed ABL depth on the LHT, it is best if the user does not provide the same WRF input file to GSI for creating LHT over a long period. In other words, the WRF input file provided to GSI as an input for creating LHT at a given time should be different than the WRF input file provided to GSI as an input for creating LHT at a time 6 h later because in that 6-h time period the ABL depth will vary. If the WRF input valid at the earlier time was also used 6 h later, the diagnosed ABL depth at the later time may have significant errors and thus the depth of the layer near the surface where LHT is not applied will not be consistent with the ABL depth. Thus, LHT may be needlessly excluded from use above the ABL or unintentionally used within the ABL. However, it should not be problematic to use the same WRF initial condition file for short periods since in general, the ABL depth should not have large variations over short periods and because even if it did, these variations are unlikely to be resolved in the coarse grid model (e.g., GFS) that is used to create the WRF input files.

For this study where LHTs were created every 15 min, WRF initial condition files were created hourly and thus the time mismatch between any LHT file and the WRF initial condition file used by GSI to create it was no more than 30 min. Note that even if one has 3-h coarse grid model data, the WRF Preprocessing System component Ungrib will temporally interpolate to create hourly data if the user sets *interval_seconds*=3600. Ultimately, one will need to execute the WRF software real.exe one time for each WRF initial condition file to be created since real.exe only creates one of these files at the beginning of the specified simulation time because initial conditions are only needed at the start of the simulation. It is not clear if GSI can process a WRF initial condition file that is not exactly at an hour.

Once the WRF initial condition files are created, the 3-D field into which GSI will place the LHT must be added. GSI requires the field to already be present in the WRF initial condition file for it to place the LHT into the file. Thus, the user should add the term and set it to zero. One way to do this is via the NetCDF Operators (NCO; http://nco.sourceforge.net) software component ncap2. For example:

```
ncap2 -s
'RAD_TTEN_DFI=T;RAD_TTEN_DFI=0;RAD_TTEN_DFI@description="Radar-
derived T Tendency for DFI";RAD_TTEN_DFI@units="K s-1"'
wrf_input_without_tendency wrf_input_with_zeroed_tendency.nc
```

4.3 Preparing Standard Observation Files for GSI

No method to prevent GSI from completing 3DVAR analyses was found and so a file containing standard observations was needed to provide the basis of these analyses. The 6-h GFS BUFR files are available from 1997 through the present via NCAR (https://rda.ucar.edu/datasets/ds337.0/index.html#access) and the last 10 days are available via NCEP (https://nomads.ncep.noaa.gov/pub/data/nccf/com/gfs/prod/gdas.YYYYMMDD/HH/gdas.tHHz.prepbufr.nr).[†] These files contain observations for the 6-h period surrounding their valid time (i.e., ±3 h from the valid time).

4.4 Preparing, Configuring, and Running GSI

While GSI V3.6 was used for this study, the source code needed to be altered to allow generation of the LHT. The official documentation included instructions on the modifications needed, but these modifications were insufficient to allow GSI to produce the LHT. The required changes were reported to the GSI maintainers for potential inclusion in a future release of GSI. The changes were not included in the initial release of GSI V3.7.

The GSI file *comgsi_namelist.sh* needs to be altered to allow the NOAA/GSD cloud analysis capability of GSI to generate the LHT. In the *&RAPIDREFRESH_CLDSURF* section, the following settings are relevant:

```
dfi_radar_latent_heat_time_period=15,
i_use_2mq4b=0,
i_use_2mt4b=0,
i_gsdcldanal_type=1,
i_gsdsfc_uselist=0,
i_lightpcp=0,
i_sfct_gross=0,
```

The setting *dfi_radar_latent_heat_time_period* specifies the number of minutes over which the LHT will be applied so that it can take the total heating calculated and turn that into a rate (Ks^{-1}). Thus, since in this study we applied a new radar data set every 15 min, we set *dfi_radar_latent_heat_time_period* to 15 so the full latent heating associated with the observed reflectivities is applied. However, a user may also set this value differently than the interval between radar updates to adjust the strength of the term. The default GSI value is 30 min.

[†] Here, the valid time of the file is specified in time UTC where YYYY is the four-digit year, MM the two-digit month, DD the two-digit day of month, and HH represents the two-digit hour and can be 00, 06, 12, or 18.

To accelerate the production of LHT, the number of iterations used for the 3DVAR analyses was reduced to one since we are not using the 3DVAR analyses. To do this, in the *&SETUP* section:

```
miter=1,niter(1)=1,niter(2)=1,
```

To avoid issues with time mismatches, the user may need to set the following in the *&SETUP* section:

```
offtime_data=.true.
```

Setting this value to *.true.* specifies that GSI will still use observations, even if their timestamp does not match the timestamp of the background data. If the value is not set to true, GSI can find a timestamp mismatch even when you are using a file that includes observations at the time you are creating an analysis because the valid time of the observation file is considered to be too far from the analysis time. For example, if one is using a 0600 UTC observation file to create an analysis at 0400 UTC, even though the observation file contains observations from 0300 to 0900 UTC, GSI will see this as an issue.

In addition to altering *comgsi_namelist.sh*, the user will also need to alter *run_gsi_regional.ksh*. The user must set the time the LHT is being created for via the setting *ANAL_TIME*. Another alteration required is to ensure that *refInGSI* links to the radar BUFR file. One way this can be implemented is via the following:

```
REFBUFR=${OBS_ROOT}/NSSLRefInGSI_${ANAL_TIME}.bufr
ln -s ${REFBUFR} refInGSI
```

Finally, GSI must be run once (via *run_gsi_regional.ksh*) for each time an LHT is required.

4.5 GSI Calculation of LHT

The NOAA/GSD cloud analysis in GSI can use other data sources in conjunction with radar data. The sources include surface observations, satellite cloud products, and lightning data. Since those data were not used in this investigation, details are not provided here regarding how they are processed.

GSI calculates the top of the ABL by finding the first level where virtual potential temperature is more than 1 K above the value at the lowest model level. It uses the relationship between virtual potential temperature at this level, the level below, and the surface to determine which model vertical level the ABL top is at. If this algorithm fails, then the ABL top is set to the second model level from the ground.

In the innermost model domain used in this study, the second level from the ground is at approximately 47 m.

The radar-reflectivity input to GSI is on specific height levels. This is interpolated to the heights on which GSI is completing analyses (the WRF levels). GSI then attempts to hypothesize what reflectivities exist below the bottom of the radar coverage so that it can replace the missing reflectivities with reflectivities consistent with those measured within the vertical extent of radar coverage. This allows GSI to calculate an LHT below the bottom of the radar coverage and thus apply a more vertically consistent profile of LHT. GSI hypothesizes values of reflectivity in profiles where nonmissing reflectivity values extend at least down to the middle WRF sigma level (and missing reflectivity values extend above the ABL), and the maximum column reflectivity exceeds 19 dBZ. In these profiles, the maximum column reflectivity is used to build a reference reflectivity profile that is interpolated to the heights of the analysis. The measured reflectivity at the lowest level within the radar coverage (i.e., the level above the first missing level) is compared to the reference reflectivity profile; we will refer to this difference as Y. If this difference Y is less than 10 dBZ, then the reference reflectivity profile is applied over its range (750–12,000 m AGL) but the entire reference reflectivity profile is adjusted by Y; that is, if Y = 5 dBZ then 5 dBZ is added to the reference reflectivity profile at each level to determine the reflectivity that replaces the missing reflectivity. If the difference Y is larger than 10 dBZ, then instead of using the reference reflectivity profile, reflectivities below the bottom of the radar coverage are set to a constant value, namely the reflectivity measured at the bottom of the radar coverage (i.e., at the first nonmissing level). After all of these processing steps are carried out, the radar reflectivity within the ABL is then set to missing.

To calculate the LHT, first calculate the reflectivity factor converted to rain/snow condensate (*$f[Z_e]$*):

$$f[Z_e] = \frac{1}{264083} * 1.5 * 10^{(Z/17.8)}, \tag{1}$$

where

Z = radar reflectivity

Then the *LHT* is calculated using the following equation:

$$LHT = \left(\frac{dT}{dt}\right)_{LH} = \left(\frac{1000}{p}\right)^{R_d/c_p} * \frac{(L_v+L_f)(f[Z_e])}{t_c c_p}, \tag{2}$$

where:

p = pressure (hPa)

R_d = dry gas constant (≈287.059)

c_p = specific heat of dry air at constant p (≈1004.705)—note that R_d/c_p is 1/3.5

L_v = latent heat of vaporization at 0° C (2.501E6 J kg^{-1})

L_f = latent heat of fusion at 0° C (0.3335E6 J kg^{-1})

t_c = time period of condensate formation (in seconds, converted from the minutes value set by the user in the GSI namelist for *dfi_radar_latent_heat_time_period*; if not set by the user, this defaults to 30 min)

$f[Z_e]$ = reflectivity factor converted to rain/snow condensate

LHT is set to zero if

- Echoes are weak: Radar reflectivity does not equal or exceed 0.001 dBZ. Also, it is set to zero throughout a column if after three horizontal smoothings of LHT (yielding $\mathrm{LHT_{smooth}}$), no vertical layer in a column of LHT exceeds 0.00002 Ks^{-1}.
- Bright banding may be a problem: Temperature is >277.15 K while reflectivity is <28 dBZ (and it is suspected this criterion is included in GSI to deal with bright banding but is not known for certain).
- Near the surface: Within the deeper of 1) the ABL and 2) the lowest six model levels.

In addition, LHT is limited to the range –0.1 Ks^{-1} to +0.1 Ks^{-1}. However, it is not clear there is a way for the value to be negative and so effectively it appears to be limited to the range 0.0 to 0.1 Ks^{-1}. If there are no data available to determine the tendency term, it is set to missing (which is signified by setting it to –20).

In the top level of the field where LHT is stored, a flag is stored indicating whether convection should be suppressed in cumulus parameterizations (see Section 4.7 for more information on this suppression). This flag is set to indicate a) insufficient information is available to set the flag (–10; i.e., missing), b) no convection in the column (0), or c) there may be convection in the column (1). It is assumed to be missing unless $\mathrm{LHT_{smooth}}$ is nonmissing for at least a 300-hPa-thick layer and there is at least one level in that layer where $\mathrm{LHT_{smooth}}$ ≥0.00002 Ks^{-1}.

4.6 Preparing GSI Output for Use in WRF

GSI creates one WRF initial condition file named *wrf_inout* for each time it is executed. The *wrf_inout* file contains the *wrfinput_dXX* file, provided as input to GSI but then altered based on the GSI 3DVAR analyses and with the radar-derived LHT included. Since we are only interested in the radar-derived LHT, we extract that field from each time to create a file containing only that field.

To extract the radar-derived LHT (RAD_TTEN_DFI), use the NCO component ncks as follows to create a file *rad_tten_dfi_temp.nc* that contains only the LHT:

```
ncks –v RAD_TTEN_DFI,Times wrf_inout rad_tten_dfi_temp.nc
```

We must now modify the timestamp of this file, if needed. Since the time of the WRF initial condition file provided to GSI (and the analysis time specified to GSI) is exactly on the hour, the rad_tten_dfi_temp.nc file will have a timestamp exactly on the hour even if it is not valid exactly on that hour. Additionally, and importantly, the timestamp in the file should be set **not necessarily to the valid time of the radar data but to the time at which we want to start using the heating term**. For a radar-reflectivity field valid at Time X, the LHT we calculate is based on the amount of heating associated with the creation of the radar reflectivity field at Time X. Thus, we want to apply that heating in the time leading up to Time X so that by Time X all of the needed heating has been applied and, hopefully, the modeling reflectivity matches that observed at Time X. If we are using 15-min radar data, as we are in this study, then if we have the 1830 UTC radar field we want to set the time of the file to 1815 UTC using the NCO component ncap2 as follows:

```
ncap2 -O -s 'Times(0,0:18)="2018-04-02_18:15:00"'
rad_tten_dfi_temp.nc rad_tten_dfi_20180402_1815UTC.nc
```

Now combine the *rad_tten_dfi** files from all of the times needed for this simulation using the NCO component ncrcat:

```
ncrcat rad_tten_dfi_*UTC.nc rad_tten_dfi_d03.nc
```

Since we are not using the GSI 3DVAR analyses we use the *wrfinput_dXX* file provided to GSI as the WRF initial condition file. If the user wanted to leverage the GSI 3DVAR analyses, the *wrf_inout* file created by GSI at the initial WRF time could be used as the WRF initial conditions file (in this case the user may want to remove the RAD_TTEN_DFI field after the *wrf_inout* file is moved to *wrfinput_dXX* so there is no chance that RAD_TTEN_DFI is read from this file).

4.7 WRF Use of LHT

While the standard version of WRF V3.9.1.1 can use LHT, it can only do so in conjunction with the DFI. However, we do not want to apply DFI, since in applying LHT to 3-km HRRR simulations, the developers of that system found it problematic to apply DFI as it smoothed out realistic structures at that scale; therefore, they did not apply DFI. Since we are running at an even higher resolution (1-km horizontal grid spacing) than HRRR, we modify WRF to be able to use LHT while not using DFI. To use LHT without DFI, WRF still must be compiled with radar DFI capabilities via setting an environmental variable (*WRF_DFI_RADAR=1*) or passing the option *radardfi* to the configure script. To enable the use of LHT without DFI, the *radar_lh_tend* option was introduced.

WRF was modified so if the LHT field was not present it would set LHT to missing rather than the default setting of 0. Setting it to 0 indicates there is no convection present; thus, if LHT is enabled, WRF would work to suppress convection across the entire domain.

While LHT use is active, at locations where LHT is not marked as missing, 3-D LHT is used in place of the temperature tendency term calculated by the microphysics scheme. Thus, there are three possible scenarios for each model grid cell:

1) The radar indicated sufficiently large reflectivities to result in a positive LHT (subject to the previously discussed conditions). This positive LHT is applied to initiate convection where the model may not have previously predicted convection. The temperature tendency predicted by the microphysics scheme is ignored as the model may not have previously been predicting convection and thus the microphysics-produced heating term may have been zero or at least smaller than the LHT. As discussed later in the report, an option was added (*radar_lh_tend_ref_limit)* that allows the user to specify that in the current scenario, if the model-predicted reflectivity exceeds the observed reflectivity, the LHT applied is set to zero to not further strengthen already-too-strong convection.

2) The radar indicated sufficiently weak reflectivities to result in a zero LHT. The temperature tendency predicted by the microphysics scheme is ignored so that if the model is predicting convection the radar indicates does not exist, the removal of the microphysics heating term will hopefully suppress the convection.

3) No radar data are available for the grid cell and so the microphysics heating term is applied normally to predict convection as it would if LHT was not being ingested at all.

Code was added to WRF to allow the user to more strongly suppress erroneous convection. The user can specify a heating term (*radar_lh_tend_when_fp*) to apply in cases where LHT is effectively zero, but the temperature tendency term from the microphysics scheme is positive; the user would presumably set this to a small negative value to more effectively suppress convection.

Code was also added to WRF so the user can choose (via *radar_lh_tend_ref_limit*) to have the LHT term not be applied at grid points where the current model-predicted reflectivity exceeds the radar-observed reflectivity equivalent to the LHT term. The goal of this setting is to prevent overstimulation of convection via the LHT term. The LHT term is set to zero when model-predicted reflectivity exceeds the observed value. Thus, if the model is already predicting convection stronger than observed, by setting this term to zero the convection is damped to allow the strength to be weakened to more closely match observations. The user must specify *radar_lh_gsi_length* to be consistent with the GSI setting *dfi_radar_latent_heat_time_period* so that the conversion from LHT to observed reflectivity can be properly carried out. To save computational expense, the user can also choose not to recalculate model-predicted reflectivity at every timestep (*radar_lh_tend_dbz_int*). Note that these options are only available when using the microphysics scheme WSM6 or Thompson and the user must have *do_radar_ref=1* set in the *&physics* section.

In addition to the replacement of the microphysics temperature tendency term with LHT, if a cumulus parameterization is used, the cumulus parameterization's potential temperature tendency will be set to zero if $1.0e\text{-}7 \leq \text{LHT} \leq 10\ \text{Ks}^{-1}$. In this study, no cumulus parameterization was used on the model domain on which LHT was applied and so this aspect was not relevant.

Additionally, for specific cumulus parameterizations, the cap suppression flag described earlier is applied. This is currently applied to the Grell 3-D scheme and the Grell–Frietas scheme. In addition to being applied while the LHT is applied, the cap suppression flag can also be applied for a period after the period of LHT application finishes. Previously, this additional time period was 31 timesteps, whereas WRF was modified so that the period is a user-specified length of time set via *radar_lh_cu_suppress_end*. This capability does not affect this study because no cumulus parameterization was used in this study on the 1-km domain where LHT was applied.

4.8 Running WRF with the LHT

Since the standard version of WRF V3.9.1.1 can only use LHT in conjunction with DFI, the description here is in regard to running LHT in the modified version of WRF V3.9.1.1 used for this study.

The user must configure WRF to read in the file with the LHT. The WRF configuration file *namelist.input* should have the following settings included in section *&time_control* for a 3-domain simulation in which LHT is applied only to the third domain:

```
iofields_filename = "iofields_blank.txt", "iofields_blank.txt",
"iofields.txt",
ignore_iofields_warning = .TRUE.,
io_form_auxinput17 = 2,
auxinput17_interval = 999999, 999999, 15,
auxinput17_inname = "rad_tten_dfi_d<domain>.nc",
auxinput17_end_m = 0, 0, 60,
```

These settings specify that auxiliary input Stream 17 is in netCDF format (*io_form_auxinput17*), is to be read from every 999999 minutes for Domains 1 and 2, but every 15 min for Domain 3 (*auxinput17_interval*). The files to be read are named *rad_tten_dfi_d<domain>.nc* where <domain> is the two-digit one-based domain number (*auxinput17_inname*), and the last time WRF should read in this input stream is at 0 min for Domains 1 and 2 and 60 min for Domain 3 (*auxinput17_end_m*).

The settings also specify that WRF should adjust which input/output (I/O) streams are used for which fields by checking *iofields_blank.txt* for Domains 1 and 2 and *iofields.txt* for Domain 3 (*iofields_filename*). If there are problems with ingesting the files in *iofields_filename*, the setting *ignore_iofields_warning=.TRUE.* indicates this should not cause a fatal error. The user should not create the file *iofields_blank.txt* (since we do not need to adjust I/O streams for those domains as we are not applying LHT to those domains) but should create *iofields.txt* with the following contents:

```
-:i:0:RAD_TTEN_DFI
+:i:17:RAD_TTEN_DFI
+:h:0:RAD_TTEN_DFI
```

The first line indicates the LHT field (RAD_TTEN_DFI) should not be read in via input Stream 0 (the WRF initial conditions file *wrfinput_dXX*), and the second line indicates the field should be read in from auxiliary input Stream 17. The final line indicates the field should be included in the history Stream 0 (*wrfout_d0**).

In the modified version of WRF, the setting *radar_lh_tend_init_end* specifies the end of the initialization period in minutes and indicates when the LHT-related code switches from behaving according to the option specified via *radar_lh_tend_init* and instead begins behaving according to the option specified via *radar_lh_tend_final*. For this study, the following were used:

```
radar_lh_tend_init = 0, 0, 1
radar_lh_tend_final = 0, 0, 2
```

The settings specified that the LHT-related code is not used on Domains 1 and 2 (since it is set to 0), but that on Domain 3 it would initially apply the LHT (since it was set to 1); then, during the rest of the simulation it would not apply LHT directory, but potentially enable the convective suppression in the cumulus parameterization (since it was set to 2). The setting *radar_lh_cu_suppress_end* (not shown) indicates the time in minutes since the model started when the cumulus suppression via the cumulus parameterization ends (whether this is enabled is also dependent on how *radar_lh_tend_init* and *radar_lh_tend_final* are set and whether a cumulus parameterization with this capability was being used). However, since no cumulus parameterization was used on Domain 3 where LHT was applied, this setting (*radar_lh_cu_suppress_end*) was not relevant for the current study.

The user must also choose how to set the previously described settings regarding 1) limiting the LHT based on the relationship between model-predicted and observed reflectivity and 2) imposing a heating rate (that the user would presumably set to be negative) to more effectively suppress convection.

Finally, the user must execute WRF to integrate forward and create forecasted weather conditions.

4.9 Evaluation Metrics

Both subjective and objective evaluation of the results are included. The objective metrics used in this evaluation are fractions skill score (FSS) and bias.

The FSS is used to evaluate how well the model predicts the placement of convection because standard metrics such as mean absolute error (MAE) can be problematic for evaluating high-resolution forecasts of convection. This is because those metrics can fail to show the benefit of near misses. For example, consider the case where a thin line of convection is observed, and the model forecasts this line of convection with a small temporal error (i.e., a near miss) such that at any given time the observed and modeled line do not overlap. The MAE for the near miss would be identical to the MAE for a model forecast with a much larger temporal error for the line of convection. Additionally, MAE may indicate a forecast that does not even indicate any line of convection as performing better than a forecast with a small temporal error, since the MAE will penalize for not forecasting the line of convection at its actual location and will also penalize for forecasting a line of convection where it did not occur.

FSS is a neighborhood method that is applied here to compare between the model forecast and the observations to determine the fraction of grid cells exceeding a reflectivity threshold within a given neighborhood size. For a given neighborhood size, each possible neighborhood of that size within the evaluation domain is evaluated. By examining neighborhoods instead of merely comparing grid points individually, the FSS is able to include the value of near misses. A perfect forecast results in an FSS of 1.0. In this study we use an 11×11 km^2 neighborhood with a 20-dBZ threshold.

While FSS helps to evaluate how well we forecast the placement of convection, bias measures how well we forecast the percentage of the domain covered by reflectivities exceeding a threshold. (Here, we use 20 dBZ.) A perfect forecast results in a bias of 1.0 whereas a value greater than 1.0 indicates too much coverage, and a value less than 1.0 indicates too little coverage.

5. Experimental Design

Experiments were carried out for the two temporally overlapping cases described in Section 3 that investigated the value of assimilating LHT. While the forecast started at 0100 UTC on 10 Sep 2016 for Case A, and at 0600 UTC on 10 Sep 2016 for Case B, the model was integrated before these times during a preforecast time period during which the radar data were assimilated. The length of the preforecast assimilation period was varied with lengths of 1, 2, and 6 h investigated. Figure 4 demonstrates the timing of the assimilation of the radar data for a 1-h preforecast. During the preforecast, for every 15-min time period, the observed radar reflectivity from the end of the 15-min time period converted to an LHT is applied to WRF. This continues throughout the preforecast time period (0000 to 0100 UTC in this example) with the goal of creating the best possible initial conditions (for 0100 UTC in this example) so that the forecast (starting at 0100 UTC) is as accurate as possible. Note that the LHT was only applied to the 1-km WRF domain since data were only available from one radar and most of the area covered by the radar data in use were within the 1-km domain.

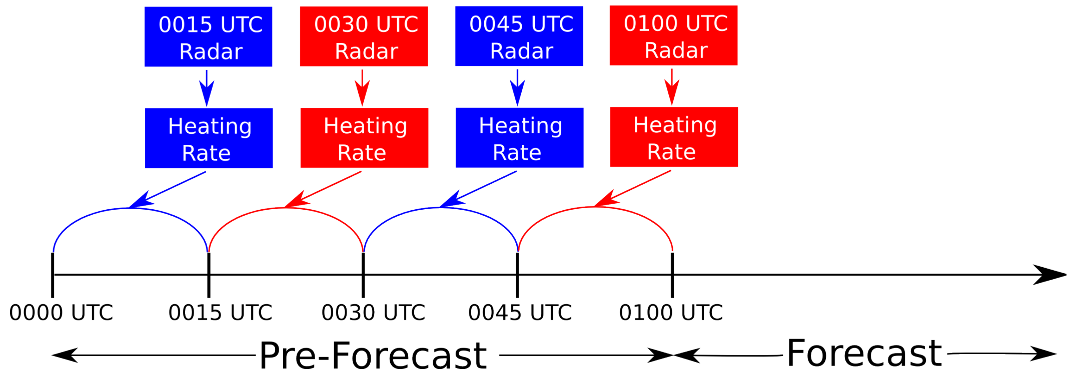

Fig. 4 In the application of radar-derived LHT in WRF, during preforecast data assimilation (here, lasting 1 h), during each 15-min period the LHT from the radar observation valid at the end of the 15 min replaces the temperature tendency from the model's microphysics parameterization

All experiments are assigned names to simplify referring to the experiments. The names consist of the following components in the order given:

- A/B: indicates Case A (0-h forecast at 0100 UTC on 10 Sep 2016) or Case B (0-h forecast at 0600 UTC on 10 Sep 2016).
- 1/2/6: indicates length of the preforecast (in hours). Note that for the experiments not applying LHT, any time simulated before the designated 0-h forecast time for the case is considered the preforecast even though observations are not being assimilated during that time period.
- Y/N: indicates whether LHT is (Y) or is not (N) applied.
- R: indicates the LHT was limited by comparisons between modeled and observed reflectivity and the presence of "R" means that *radar_lh_tend_ref_limit* was enabled. The term was calculated every 10 timesteps (*radar_lh_tend_dbz_int = 10)*.
- S: indicates that additional convective suppression was included. Namely, in this study the presence of "S" indicates that *radar_lh_tend_when_fp* was set to –0.0001 Ks^{-1}, so that when the microphysics scheme indicates a positive temperature tendency but the LHT is effectively zero, this cooling term is applied to more strongly suppress apparently erroneous convection.

6. Results

6.1 Benefits of LHT and Dependence on Preforecast Length

The HRRR implementation of LHT used a preforecast length of 1 h in which to apply the LHT and so our initial use of LHT was with a 1-h assimilation length. Figure 5 compares our WRF 0-h forecasts of reflectivity with observations for Case A (0-h forecast time of 0100 UTC [1300 MHT] on 10 Sep). For the model data, the level closest to 1-km AGL was used for comparison with the radar data processed to 1-km AGL. Integrating the model for 1 h without using LHT (Fig. 5a, Exp. A1N) results in reflectivity not exceeding 5 dBZ at this level, in contrast to the observations (Fig. 5g) that indicate regions of ≥35 dBZ. At least without applying LHT, 1 h is not long enough for the model to spin up convection. If we apply LHT for the 1-h preforecast (Fig. 5d, Exp. A1Y), reflectivities of ≥35 dBZ occur in regions of the domain, and model reflectivities ≥5 dBZ occur in areas where observations also indicate positive reflectivity values. However, the positive reflectivities are notably more widespread in the observations than in A1Y.

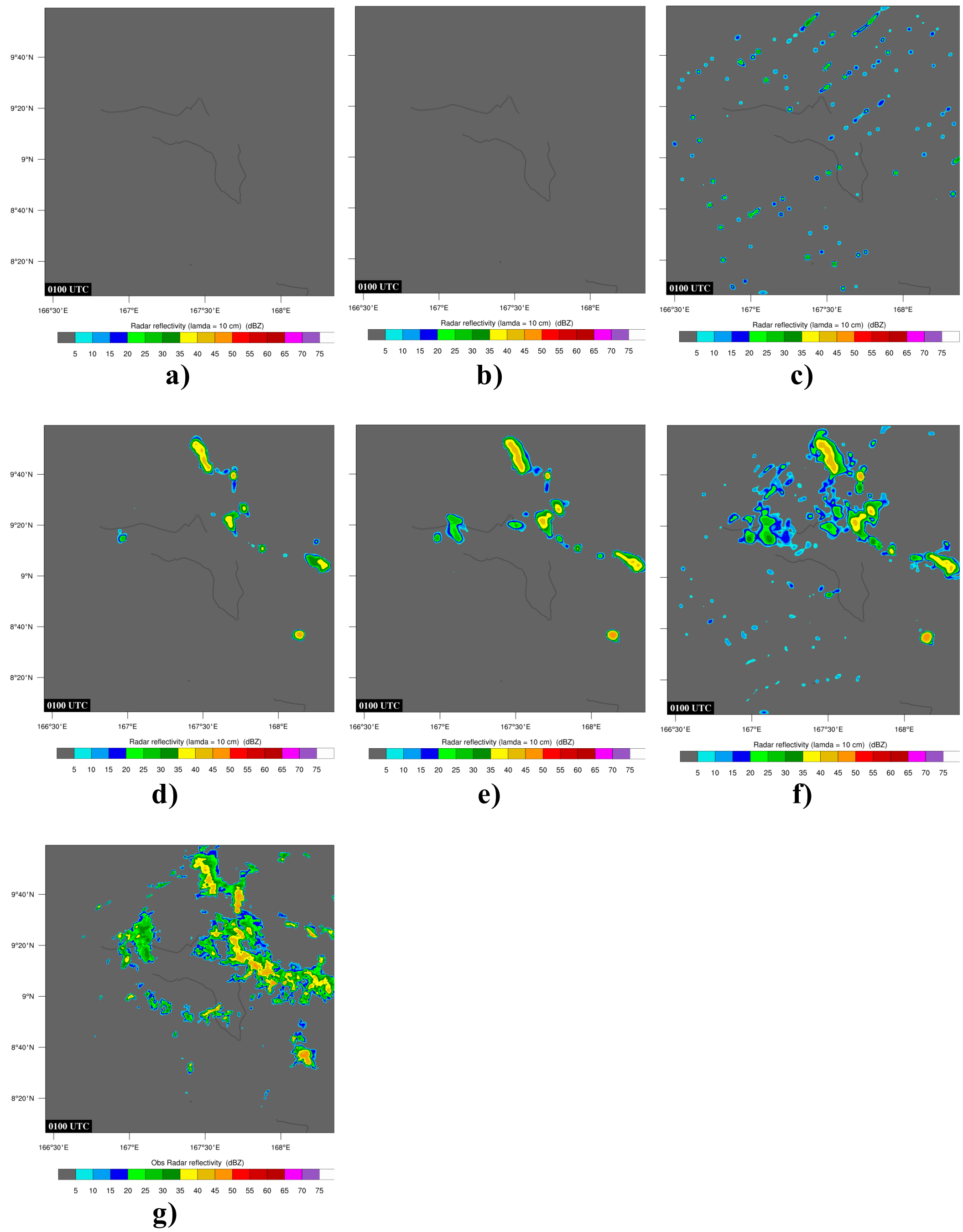

Fig. 5 Comparison of radar reflectivity from model level closest to 1-km AGL and observed 1-km AGL radar reflectivity at 0100 UTC on 10 Sep 2016: experiments are a) A1N, b) A2N, c) A6N, d) A1Y, e) A2Y, f) A6Y, and g) the observed field closest to this time; for all experiments this is the 0-h forecast but length of preforecast varies among experiments, as does whether or not LHT was assimilated.

We investigated if increasing the length of assimilation would allow the 0-h forecast to more closely match observations. Increasing the preforecast length to 2 h shows that without use of LHT, the reflectivity still does not reach 5 dBZ

(Fig. 5b, Exp. A2N). Adding use of LHT through the 2-h preforecast period (Fig. 5e, Exp. A2Y) shows somewhat more widespread convection than with the 1-h preforecast period (Fig. 5b), but still not as widespread as observations (Fig. 5g). Therefore, the preforecast length was increased to 6 h. Without use of LHT (Fig. 5c, Exp. A6N) we now have very small areas of mostly weak reflectivities but this is not at all consistent with the organization of convection observed (Fig. 5g). However, when LHT is used (Fig. 5f, Exp. A6Y), convection is more widespread than with the 1- or 2-h preforecast period, and appears to be more consistent with the observed field (Fig. 5g).

The HRRR 1-h preforecast is initialized from the 13-km hourly updated RAP model that is assimilating the network of radars over CONUS. In contrast, Kwajalein is outside the coverage of the RAP model and we are using 0.5° data from GFS, which runs a new cycle every 6 h and is not thought to be assimilating Kwajalein radar data. Thus, while a 1-h preforecast may perform well for HRRR, it does not appear sufficient for these 1-km simulations over Kwajalein Atoll.

Moving from the 0-h forecast (Fig. 5) to the 1-h forecast (Fig. 6), using the same experiments, allows an evaluation of whether the convection introduced via the LHT maintains itself after the LHT is removed. Assimilation of radar-reflectivity data can result in the introduction of hydrometeors that are not supported dynamically in the model and thus disappear as soon as the forcing from data assimilation is removed. However, in this case it is clear that after 1 h the hydrometeors introduced via the LHT remain even though the LHT is no longer being applied.

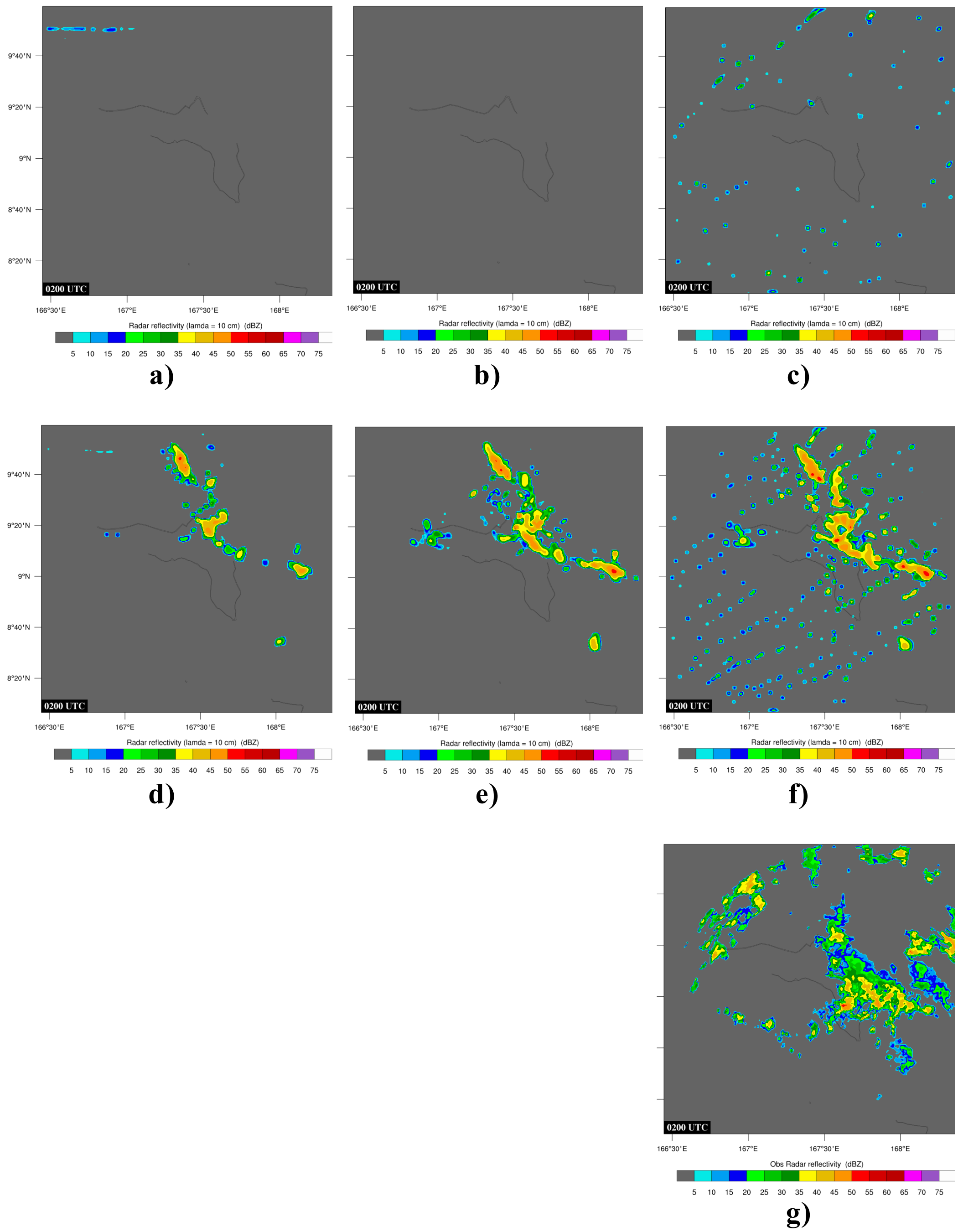

Fig. 6 Comparison of radar reflectivity from model level closest to 1-km AGL and observed 1-km AGL radar reflectivity at 0200 UTC on 10 Sep 2016: experiments are a) A1N, b) A2N, c) A6N, d) A1Y, e) A2Y, f) A6Y, and g) the observed field closest to this time; for all experiments this is the 1-h forecast but length of preforecast varies among experiments, as does whether or not LHT was assimilated.

An objective evaluation of how the preforecast length affects the ability to forecast the placement of convection is seen in the FSS time series in Fig. 7a. Note that the x-h lead time on the x-axis is equivalent to the x-h forecast time. Thus, the 0-h forecast is at left edge of the figure where it is labeled as having a 0-h lead time. The longer the preforecast assimilation period, the higher the FSS during the first 3 h of the forecast. At the 0-h forecast, the FSS is <0.4 for the 1-h preforecast (A1Y) but >0.7 for a 6-h preforecast (A6Y). Between 3 and 4 h into the forecast the various preforecast lengths begin to have very similar FSS values and thus there is no longer added value to a longer preforecast data-assimilation period in terms of convection placement.

However, the time series of bias (Fig. 7b) indicates that longer preforecast usually produces biases closer to 1 through the first 8 h of the forecast. During the first 2 h, increasing preforecast length clearly improves the bias. For example, at 1 h into the forecast, a 1-h preforecast (A1Y) leads to a bias of approximately 0.25, a 3-h preforecast (A3Y) leads to a bias approximately 0.50, and a 6-h preforecast (A6Y) leads to a bias approximately 0.75. After the first 2 h, while longer preforecasts usually lead to better biases through the first 8 h, the differences among the experiments vary substantially.

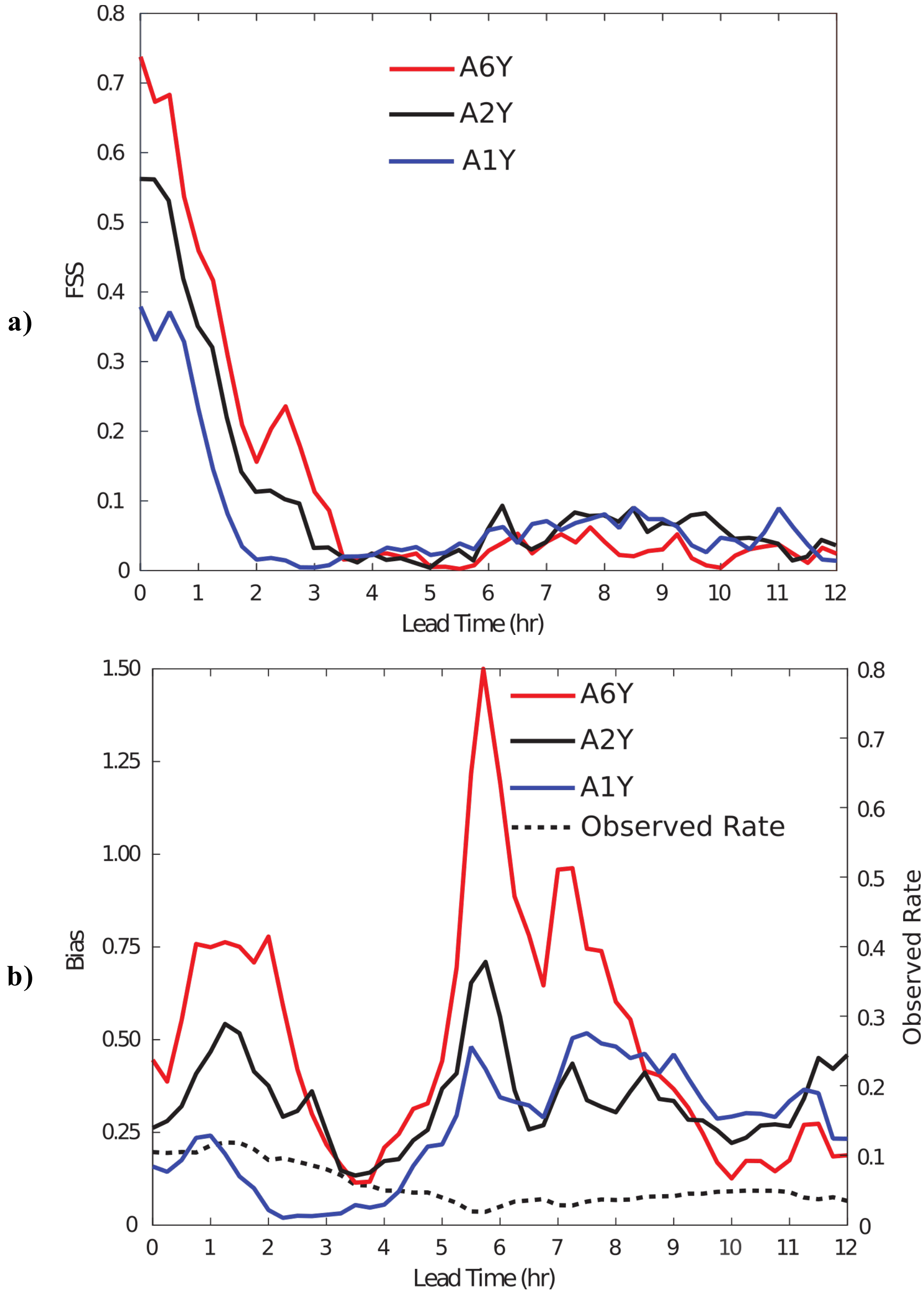

Fig. 7 Time series for Case A of a) FSS using an 11 × 11 km^2 neighborhood and b) bias and observed rate (all using a 20-dBZ threshold): FSS and bias are for experiments using LHT for various lengths of time; note the x-h forecast is equivalent to x-h lead.

While the previous plots (Fig. 7a, b) illustrate the differences in the accuracy of the forecast from varying the length of the preforecast assimilation period, Fig. 8 shows the value of using the best-performing preforecast length (6 h, A6Y) compared with not applying the radar-derived LHT at all (A6N). For the first portion of the forecast the difference caused by using LHT is large. For FSS, with LHT the FSS starts >0.70, whereas without LHT it starts at approximately 0.05. The two experiments have roughly equivalent FSS starting a little after 3 h into the forecast. For bias, with LHT the bias starts at approximately 0.45 but rises to approximately 0.75 and stays near that value until after 2 h into the forecasts, whereas without LHT the bias starts at approximately 0.10 and remains there for the first 3 h. After 3 h the magnitude of the biases of the two experiments are similar for a short time before it shifts to the experiment with LHT (A6Y) having bias with a higher magnitude (and almost always closer to the perfect bias of 1.00) until about 9 h into the forecast. Thus, the use of LHT benefits the placement of convection (as measured by FSS) through the first 3 h of the forecast and benefits the overall coverage of convection (as measured by bias) for at least the first 3 h, but then also for the 5–9-h forecast.

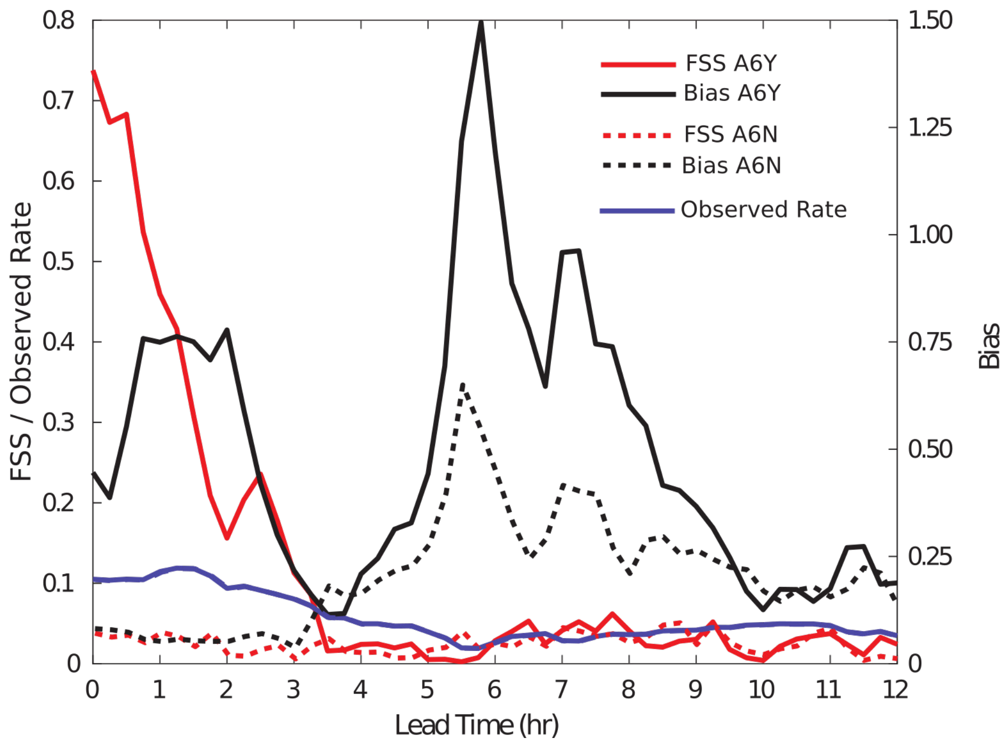

Fig. 8 Time series of FSS (left axis) and bias (right axis) for experiments during Case A having a 6-h preforecast with use of LHT (A6Y) and without use of LHT (A6N); proportion of domain observed to exceed the reflectivity threshold (20 dBZ) is also plotted using left axis

The results of Case B (0-h forecast at 0600 UTC [1800 MHT] on 10 Sep 2016) will now be evaluated to determine how similar these results are to those of Case A. In Fig. 9a, the 2-h (B2Y) and 6-h (B6Y) preforecast periods produce higher FSS than the 1-h preforecast period (B1Y) as in Case A. However, unlike the clear benefit seen in Case A for the 6-h preforecast period compared to the 2-h preforecast period

(Fig. 7a), in Case B, while the 6-h preforecast performs better than the 2-h preforecast at the 0-h forecast, the 2-h preforecast performs better than the 6-h preforecast period in terms of FSS during the rest of the first hour of the forecast. While the differences in FSS among the preforecast times lasted for the first approximately 3 h in Case A, in Case B the difference appears to cease after the first 1 h. Finally, the magnitude of the FSS even at the 0-h forecast is lower in Case B (0.1–0.4) than Case A (0.4–0.7).

In terms of bias, in Case B (Fig. 9b) the bias overall improves with increasing preforecast length for the first approximately 4 h. Besides a spike in bias during part of the first hour, during the first 4 h bias remains between approximately 0.65 and 1.10 for the 6-h preforecast length. In contrast to this, for the 2-h preforecast, bias remains between approximately 0.15 and 0.40 for the first 3 h and between approximately 0.00 and 0.20 for the 1-h preforecast; in both the 1- and 2-h preforecasts, the magnitude of bias increases to 0.50–0.55 by 4 h into the forecast. For the 5–6 h forecast, the three experiments have similar biases, after which the 1- and 2-h preforecast lengths have biases whose magnitude is larger and generally closer to the desired 1.00 value than the 6-h preforecast for the remainder of the simulation. Compared with Case A (Fig. 7b), bias in Case B is often closer to 1.00 and has a higher magnitude during the first 4 h for the 6-h preforecast (B6Y vs. A6Y). Both cases show the magnitude of bias increasing with preforecast length (and usually increasing to a value closer to 1.00 and thus better) during the beginning of the forecast, but this difference between the 6-h and the shorter preforecast times is larger in Case B and lasts longer (although in Case A the difference eventually reappears and the second instance lasts until well after the initial instance in Case B ends).

a)

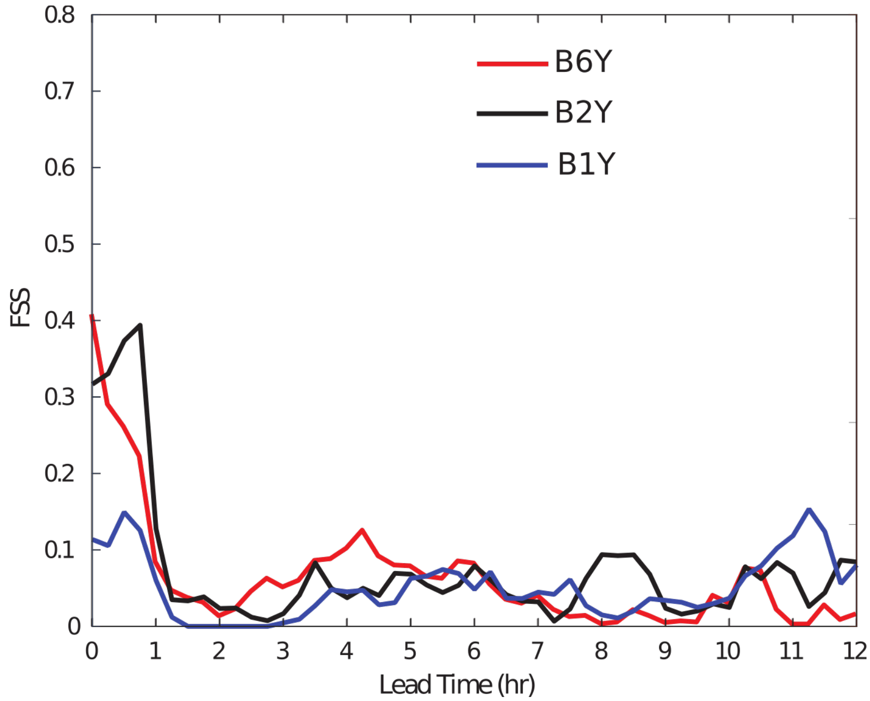

b)

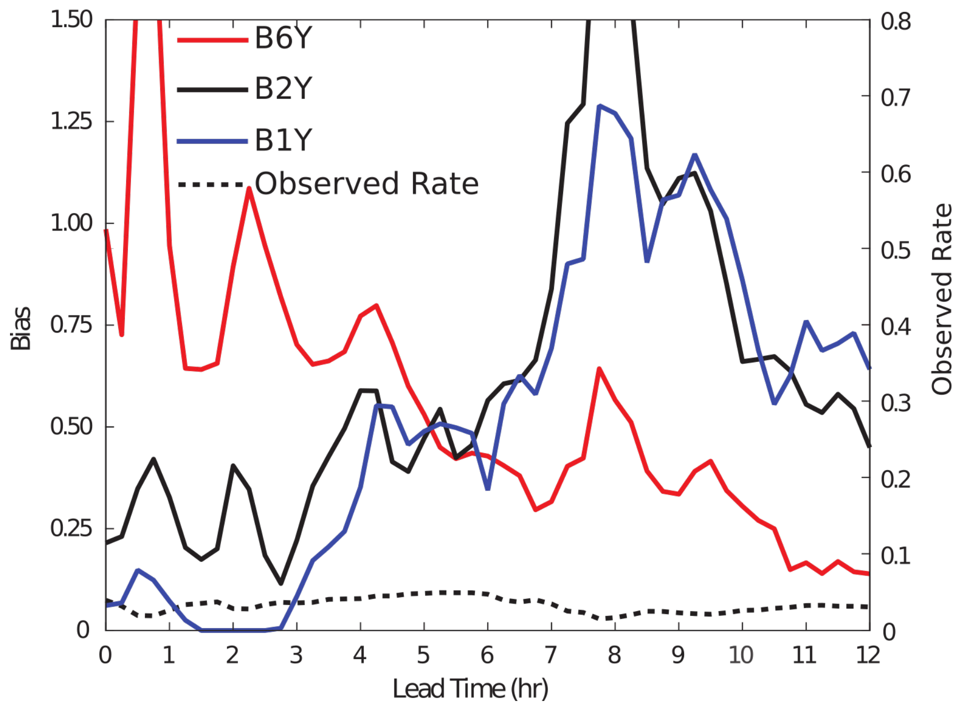

Fig. 9 Time series for Case B of a) FSS using an 11 × 11 km^2 neighborhood and b) bias and observed rate (all using a 20-dBZ threshold); FSS and bias are for experiments using LHT for various lengths of time

The benefit of assimilating radar data (LHT) during a 6-h preforecast (B6Y) is examined via comparison against an experiment with a 6-h preforecast without LHT (B6N, Fig. 10). The equivalent figure for Case A is Fig. 8. In Case B, in terms of placement of convection (FSS), the benefit of LHT lasts about 1 h; this is much shorter than the 3 h seen for Case A (A6Y vs. A6N in Fig. 8). To better understand potential reasons for this difference we examine the observed reflectivity fields at the 0-h forecast times for these experiments. In Case A (e.g., A6Y), the 0-h forecast time is 0100 UTC (1300 MHT), whereas in Case B (e.g., B6Y), the 0-h forecast time is 0600 UTC (1800 MHT). In Fig. 2, at 0100 UTC, organized areas of convection with reflectivity ≥35 dBZ are seen. One hour later (0200 UTC), although convection has evolved, areas of organized convection remain that are clearly associated with the convection seen an hour earlier. Organized convection of nontrivial strength persisting over time provides an opportunity for 0-h forecasts improved by LHT to result in continued improvements as the forecast evolves. In Case B, the observed reflectivity at the 0-h forecast time (0600 UTC, Fig. 2) shows a north–south-oriented area of reflectivity with very limited areas having reflectivities exceeding 30 dBZ. While there are some other areas of returns with very limited locations reaching 35 dBZ, in general the returns are weaker and less widespread than at the 0-h forecast of Case A. One hour later (i.e., the 1-h forecast in B6Y and B6N), the area of returns in the center of the domain has almost disappeared and thus there are limited structures seen in the reflectivity whose 1-h forecast we can improve via the assimilation of radar–reflectivity-derived latent heating. This difference in the strength, spatial coverage, and temporal continuity of reflectivity elements between Case A and Case B appears to explain the drastic differences in the magnitude of FSS at the 0-h forecast time and in the length of time over which LHT benefits FSS. It is harder to correctly forecast the placement of reflectivity structures when they are weak and do not last long.

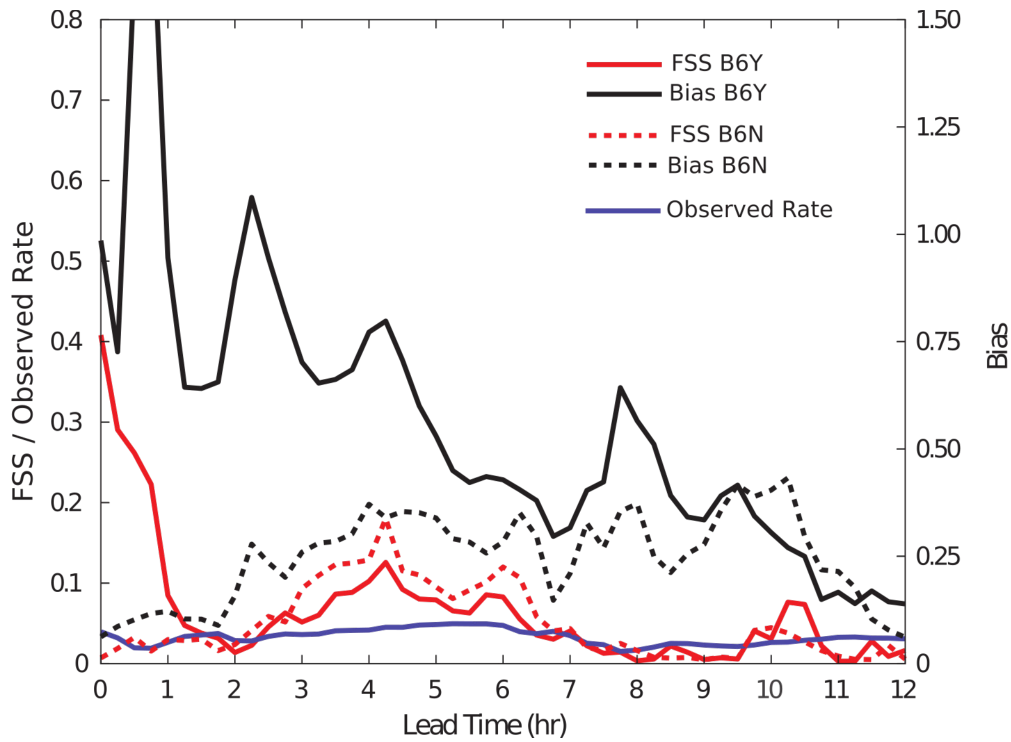

Fig. 10 Time series of FSS (left axis) and bias (right axis) for experiments during Case B having a 6-h preforecast with use of LHT (A6Y) and without use of LHT (A6N); proportion of domain observed to exceed the reflectivity threshold (20 dBZ) is also plotted using left axis

In terms of bias, benefits of LHT appear to last until about 9 h into the forecast (although experiments with shorter preforecast lengths showed better bias in the 9–12 h forecast). The length of time over which bias is overall improved with a 6-h preforecast data-assimilation period is similar to Case A, with the caveats that 1) in Case A there was a period around 3–4 h when the biases between the experiments were very similar and 2) there is a spike in bias in the period just before the 1-h forecast in Case B that is not present in Case A.

6.2 Reflectivity Limiter and Cooling Term

Because we are applying LHT over a much longer period (6 h) than used in previous work (1 h in HRRR), it may be that application of LHT could overstimulate convection. In the nudging data-assimilation technique, the nudging–diagnosed tendency that is imposed evolves with time since it is based on a comparison of the observed quantity to the modeled quantity at (or near) the time at which the nudging term is applied. Thus, as the modeled quantity evolves in time, the nudging term for a given observation varies in time; it is larger when the modeled value differs more from the observation and smaller when the modeled value differs less from the observation. This means that when the modeled value matches the observed value, the nudging term goes to zero. However, with the technique used to apply

LHT, for a given reflectivity observation the same heating term is applied to the model regardless of the reflectivity forecast by the model. This means that the same heating term will be applied to the model whether the model predicts a reflectivity much lower or much higher than the observation. Since the radar-derived latent heating term replaces the term calculated by the model's microphysics scheme, this may provide a method to damp overenthusiastic model convection, but it may be more effective to set the LHT to zero in locations where the model is overpredicting convection. This technique was applied in A6YR and B6YR.

By comparing model forecasts with and without the reflectivity limiter, the effects of this technique can be evaluated. For Case A, the effects of applying the reflectivity limiter can be seen in Fig. 11 by comparing without the limiter (A6Y) and with the limiter (A6YR) for FSS (Fig. 11a) and bias (Fig. 11b). Overall, the results appear to be very similar. In general, the bias is below 1.0 before the reflectivity limiter and so there may not have been an issue with overprediction due to overstimulation in this case. There is a small decrease in overprediction around forecast hour 5.75 with application of the reflectivity limiter, but since this is well into the forecast, this difference may not be important. Figure 12 is the equivalent figure for Case B (as Fig. 11 is for Case A) and here there is a more noticeable impact during the beginning of the forecast. The use of the reflectivity limiter decreases an overprediction bias in the second half of the first hour of the forecast (in Fig. 12b B6YR with the reflectivity limiter compared to B6Y without the limiter). However, it also results in the model underpredicting more than without the limiter in the first 15 min of the forecast. The FSS does improve with the use of the limiter during the first hour of the forecast, indicating the model does better placing the convection. The results of applying the reflectivity limiter for these cases suggest that there may be benefit to this technique, but testing over additional cases is necessary to determine whether a benefit exists.

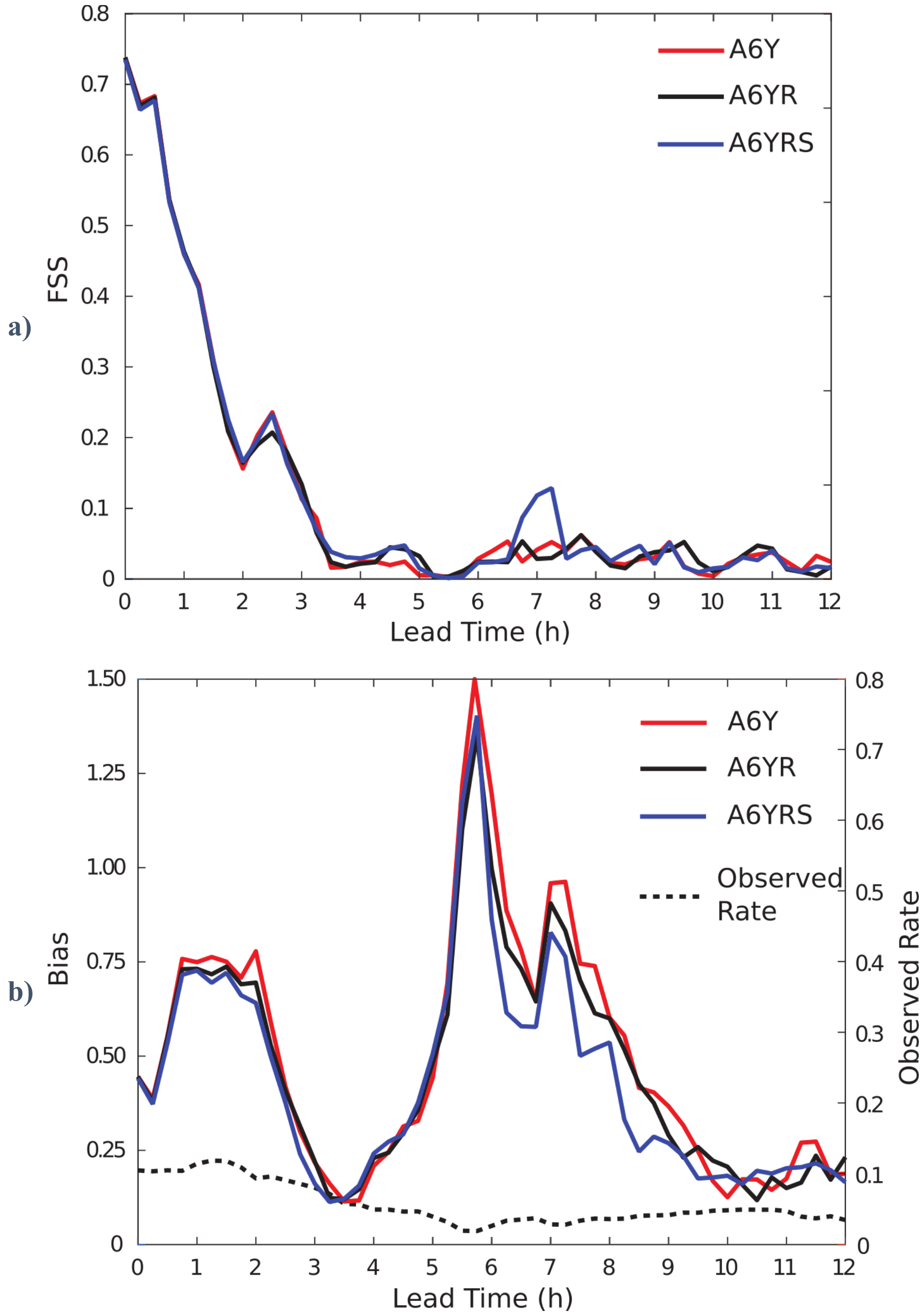

Fig. 11 Time series for Case A of a) FSS using an 11 × 11 km^2 neighborhood and b) bias and observed rate (all using a 20-dBZ threshold); FSS and bias are for experiments using LHT for 6 h and testing effects of adding reflectivity limiter (A6YR) and extra suppression (A6YRS) to standard configuration (A6Y)

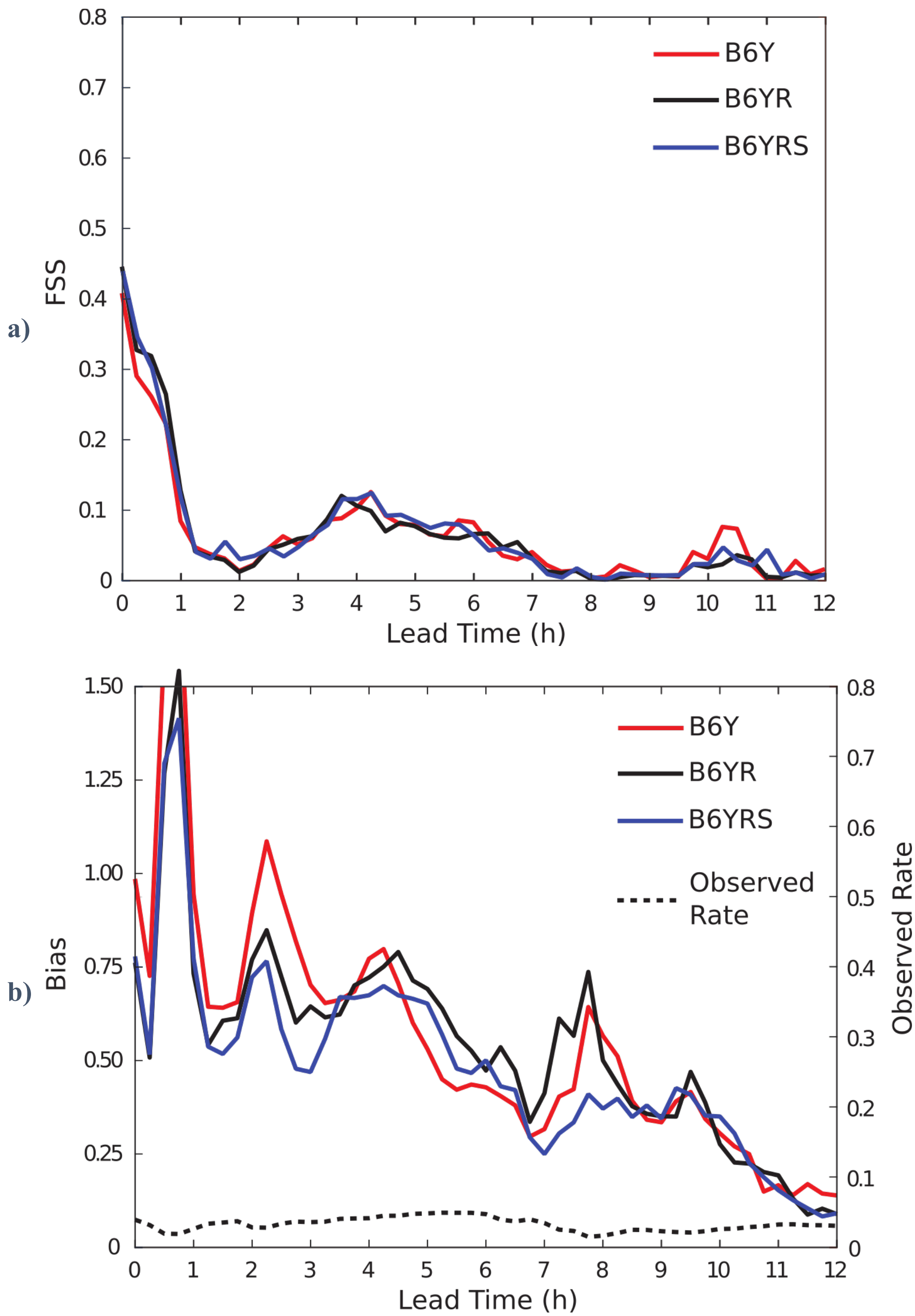

Fig. 12 Time series for Case B of a) FSS using an 11 × 11 km^2 neighborhood and b) bias and observed rate (all using a 20-dBZ threshold); FSS and bias are for experiments using LHT for 6 h and testing effects of adding reflectivity limiter (B6YR) and extra suppression (B6YRS) to standard configuration (B6Y)

Some results suggested the LHT technique was not sufficiently suppressing erroneous convection; that is, scattered weak convection in the southwestern corner of the domain at 0100 UTC in A6Y in Fig. 5f when compared to the observed field in Fig. 5g. Thus, in an effort to more effectively suppress convection, in cases where the model's microphysics schemes indicated a nonzero temperature tendency term but the radar reflectivity suggested no heating term should be imposed, instead of merely ignoring the microphysics temperature tendency term, a small cooling term is introduced. However, applying this technique resulted in very little change in verification statistics in Case A (A6YR without the cooling term and A6YRS with cooling term for FSS [Fig. 11a] and bias [Fig. 11b]) or Case B (B6YR without cooling term and B6YRS with cooling term for FSS [Fig. 12a] and bias [Fig. 12b]). There is some amount of worsening of the underforecasting bias in Case B for much of the 2–8-h forecast, but the importance of this difference is unclear. Overall, it may be that the cooling term of 0.0001 Ks^{-1} was insufficiently strong to have an effect, or that areas where additional suppression is needed are very limited and thus effects of applying this modification are not seen in the verification statistics.

In regard to the erroneous scattered weak convection in Fig. 5f, the chosen verification statistics are not likely to measure effects of the additional suppression on these since they appear to generally be weaker than the 20-dBZ threshold used to calculate verification. However, comparison of the model A6YR and A6YRS reflectivity fields at 0100 UTC (not shown) suggest the suppression term has done little to suppress this erroneous convection. The level being evaluated (≈1-km AGL) is very close to the GSI-diagnosed ABL top, and so the exclusion of the LHT from the GSI-diagnosed ABL may be limiting the ability of the LHT to suppress this convection.

7. Summary, Conclusion, and Future Work

Kwajalein Atoll radar reflectivity for two cases—two forecast start times on the same day—was converted to a 3-D temperature tendency and applied to WRF simulations. The 3-D temperature tendency was based on the latent heating that would have occurred to create the observed radar-reflectivity fields. The temperature tendency replaced the microphysics temperature tendency on the 1-km horizontal grid spacing domain and had substantial positive impact on the short-term reflectivity forecast. The impact was measured in terms of improvements in the placement of convection (via the neighborhood method FSS) and the overall coverage of convection (bias) using a neighborhood size of 11 × 11 km^2 and a reflectivity threshold of 20 dBZ. These results indicated improvements in the placement of convection were substantial, but persisted much longer (≈3 h vs. <1 h) for the case with more widespread, stronger convection (Case A) compared with the other case (Case B). Improvements in bias appear to last perhaps approximately 9 h; this is much longer than improvements in predictions of convection placement.

The benefits were overall largest with the longest preforecast time period over which a series of reflectivity observations was assimilated. Prior application of this technique in the operational 3-km horizontal grid spacing HRRR used a 1-h assimilation period. For our application, for these cases, a 6-h assimilation length was overall superior to 1- and 2-h assimilation lengths. Some ways in which our simulations differ from HRRR are that 1) our simulations are not over CONUS where many radars are available to assimilate, and 2) our simulations are initialized via a much coarser simulation that is updated much less frequently and presumably does not assimilate radar data over our domain. These differences appear to require a longer assimilation period to gain sufficient improvement from the radar data.

The benefits of modifications to the technique were unclear for the limited number of cases tested. Not applying the LHT when the model overforecast reflectivity did result in some potential improvements. Adding a cooling term to more effectively suppress erroneous convection appeared to have very little effect on verification metrics, although the metrics employed in this study would not measure suppression of erroneous weak convection. Subjective evaluation suggested that some erroneous convection remains even with use of LHT with the added suppression term because it is within or near the GSI-diagnosed ABL in which the LHT is not applied.

While the results of this study indicate the application of radar-derived LHT can substantially improve short-term forecasts of reflectivity, additional work is needed. These experiments were only carried out on two cases, and these two cases had 0-h forecast times within the same 24-h period. Testing on additional cases is needed to determine the generality of these results.

Broadening the verification applied could provide additional insights regarding the performance of the technique. While this study focused on 11- × 11-km^2 neighborhoods and a 20-dBZ threshold, evaluation at other neighborhood sizes and thresholds would be beneficial. In addition, Raby et al. (forthcoming) investigated a wavelet-based scale decomposition-verification technique that could help us better understand the scale dependence of this technique's performance.

While the version of WRF in WREN_RT has been updated to include the capability to apply this technique, WREN_RT does not have the capability to prepare the input data and run simulations with this technique. The techniques described in this report can also be applied in locations other than Kwajalein. We have used the CONUS

MRMS radar product as the basis for calculating the radar-derived latent heating term for application to WRF.

8. References

Albers S, McGinley J, Birkenheuer. The Local Analysis and Prediction System (LAPS): analyses of clouds, precipitation, and temperature. Weather Forecast. 1996;11:273–287.

Alexander C, Dowell D, Hu M, Ladwig T, Weygandt S, Benjamin SG. Expanding use of radar data in deterministic and ensemble data assimilation for the High-Resolution Rapid Refresh (HRRR). Presented at 38th Conference on Radar Meteorology; American Meteorological Society; 2017 Aug 28–Sep 1; Chicago, IL. 19B.2. c2017. [accessed 2019 Sep 24] https://ams.confex.com/ams/38RADAR/webprogram/Paper321169.html.

Barker D. Met Office global and regional numerical weather prediction: status and plans. Global and Regional-Scale Models: Updates and Center Overviews at the 99th Annual American Meteorological Society Meeting; 2019 Jan 7–10; Phoenix, AZ.

Barker D, Huang X-Y, Liu Z, Auligné T, Zhang X, Rugg S, Ajjaji R, Bourgeois A, Bray J, Chen Y, et al. The weather research and forecasting model's community variational/ensemble data assimilation system: WRFDA. B Am Meteorol Soc. 2012;93:831–843.

Benjamin SG, Weygandt S, Brown JM, Hu M, Alexander CR, Smirnova TG, Olson JB, James EP, Dowell DC, Grell GA, et al. A North American hourly assimilation and model forecast cycle: the Rapid Refresh. Mon Weather Rev. 2016;144(4):669–1694.

Cai H, Reen BP, Raby JW. Radar data processing for GSI radar data assimilation. White Sands Missile Range (NM): CCDC Army Research Laboratory (US). Forthcoming.

Carlin JT, Gao J, Snyder JC, Ryzhkov AV. Assimilation of ZDR columns for improving the spinup and forecast of convective storms in storm-scale models: proof-of-concept experiments. Mon Weather Rev. 2017;145: 5033–5057.

Gemmill W, Katz B, Li X. Daily real-time, global sea surface temperature—high-resolution analysis: RTG SST HR. College Park (MD): NOAA/National Weather Service, National Centers for Environmental Prediction, Environmental Modeling Center; 2007. Report No.: 260.

Hong S-Y, Noh Y, Dudhia J. A new vertical diffusion package with an explicit treatment of entrainment processes. Mon Weather Rev. 2006;134(9):2318–2341. doi:10.1175/MWR3199.1.

Hong S, Lim J. The WRF single-moment 6-class microphysics scheme (WSM6). J Korean Meteorol Soc. 2006;42(2):129–151.

Iacono MJ, Delamere JS, Mlawer EJ, Shephard MW, Clough SA, Collins WD. Radiative forcing by long-lived greenhouse gases: calculations with the AER radiative transfer models. J Geophys Res. 2008;113:D13103. doi:10.1029/2008JD009944.

Jiang H, Albers S, Xie Y, Toth Z, Jankov I, Scotten M, Picca J, Stumpf G, Kingfield D, Birkenheuer D, Motta B. Real-time applications of the variational version of the Local Analysis and Prediction System (vLAPS). B Am Meteorol Soc. 2015;96:2045–2057.

Jimenez PA, Dudhia J, Gonzalez–Rouco JF, Navarro J, Montavez JP, Garcia–Bustamante E. A revised scheme for the WRF surface layer formulation. Mon Weather Rev. 2012;140:898–918. doi:10.1175/MWR-D-11-00056.1.

Jones CD, Macpherson B. A latent heat nudging scheme for the assimilation of precipitation data into an operational mesoscale model. Meteorol App. 1997;4(3):269–277.

Lawson JR, Kain JS, Yussouf N, Dowell DC, Wheatley DM, Knopfmeier KH, Jones TA. Advancing from convection-allowing NWP to warn-on-forecast: evidence of progress. Weather Forecast. 2018;33(2):599–607.

Markowski P, Richardson Y. Mesoscale meteorology in midlatitudes. West Sussex (England): John Wiley & Sons, Ltd.; 2010.

[NCAR] National Center for Atmospheric Research. User's guide for the Advanced Research WRF (ARW) modeling system version 3.9. Boulder (CO): National Center for Atmospheric Research; 2017. [accessed 2019 March 12] http://www2.mmm.ucar.edu/wrf/users/docs/user_guide_V3.9/contents.html.

Raby JW, Cai H, Reen BP, Smith JA. Application of the scale decomposition technique for assessing radar reflectivity forecasts of the Weather Running Estimate–Nowcast modeling system. White Sands Missile Range (NM): CCDC Army Research Laboratory (US). Forthcoming.

Reen BP, Xie Y, Cai H, Albers S, Dumais RE Jr, Jiang H. et al. Incorporating variational Local Analysis and Prediction System (vLAPS) analyses with nudging data assimilation: methodology and initial results. Adelphi Laboratory Center (MD): Army Research Laboratory (US); 2017 Sep. Report No.: ARL-TR-8145. https://www.arl.army.mil/arlreports/2017/technical-report.cfm?id=7957.

Reen BP, Dawson LP. The Weather Running Estimate–Nowcast Realtime (WREN_RT) system, version 1.03. Adelphi Laboratory Center (MD): Army Research Laboratory (US); 2018 Sep. Report No.: ARL-TR-8533. https://www.arl.army.mil/arlreports/2018/technical-report.cfm?id=6170.

Shao H, Derber J, Huang X-Y, Hu M, Newman K, Stark D, Lueken M, Zhou C, Nance L, Kuo Y-H, Brown B. Bridging research to operations transitions: status and plans of community GSI. B Am Meteorol Soc. 2016;97:1427–1440. doi: 10.1175/BAMS-D-13-00245.1.

Skamarock WC, Klemp JB, Dudhia J, Gill DO, Barker DM, Duda M, Huang XY, Wang W, Powers JG. A description of the advanced research WRF version 3. Boulder (CO): National Center for Atmospheric Research; 2008. Report No.: 475 [accessed 2019 Sep 4]. http://www2.mmm.ucar.edu/wrf/users/docs/arw_v3_bw.pdf.

Stephan K, Klink S, Schraff C. Assimilation of radar-derived rain rates into the convective-scale model COSMO-DE at DWD. Q J Roy Meteor Soc. 2008;134(634):1315–1326.

Tewari M, Chen F, Wang W, Dudhia J, LeMone MA, Mitchell K, Ek M, Gayno G, Wegiel J, Cuenca RH. Implementation and verification of the unified NOAH land surface model in the WRF model. In: 20th Conference on Weather Analysis and Forecasting/16th Conference on Numerical Weather Prediction; 2004 Jan 12–16; Seattle, WA. Seattle (WA): American Meteorological Society. c2004. p. 11–15.

Wang W, Warner TT. Use of four-dimensional data assimilation by Newtonian relaxation and latent-heat forcing to improve a mesoscale-model precipitation forecast: a case study. Mon Weather Rev. 1988;116(12):2593–2613.

Wang H, Sun J, Fan S, Huang X. Indirect assimilation of radar reflectivity with WRF 3D-VAR and its impact on prediction of four summertime convective events. J Appl Meteorol Clim. 2013;52:889–902.

Xiao Q, Sun J. Multiple-radar data assimilation and short-range quantitative precipitation forecasting of a squall line observed during IHOP_2002. Mon Weather Rev. 2007;135(10):3381–3404.

Zhang J, Howard K, Gourley JJ. Constructing three-dimensional multiple radar reflectivity mosaics: Examples of convective storms and stratiform rain echoes. J Atmos Ocean Tech. 2005;22:30–42.

Zhang C, Wang Y. Projected future changes of tropical cyclone activity over the western North and South Pacific in a 20-km-mesh regional climate model. J Climate. 2017;30:5923-5941.

List of Symbols, Abbreviations, and Acronyms

3-D	3-dimensional
3DVAR	3-dimensional variational
4DVAR	4-dimensional variational
ABL	atmospheric boundary layer
AGL	above ground level
ARL	Army Research Laboratory
AvMC	Aviation and Missile Center
BUFR	Binary Universal Form for the Representation of meteorological data
CCDC	US Army Combat Capabilities Development Command
CONUS	continental United States
DFI	digital filter initialization
EnKF	ensemble Kalman filter
FSS	fractions skill score
GFS	Global Forecast System
GSD	Global System Division
GSI	Gridpoint Statistical Interpolation
HRRR	High-Resolution Rapid Refresh
I/O	input/output
LHT	latent heating temperature tendency terms
MADIS	Meteorological Assimilation Data Ingest System
MAE	mean absolute error
MET	Model Evaluation Tools
MHT	Marshall Islands time
MM5	Pennsylvania State University–NCAR mesoscale model Version 5

MRMS	multiradar multisensor
NASA	National Aeronautics and Space Administration
NCAR	National Center for Atmospheric Research
NCEP	National Centers for Environmental Prediction
NCO	NetCDF Operators
NOAA	National Oceanic and Atmospheric Administration
NWP	numerical weather prediction
PBL	planetary boundary layer
RAP	Rapid Refresh
RRTMG	rapid radiative transfer model for general circulation models
UF	Universal Format
UKMET	United Kingdom Met Office
UTC	coordinated universal time
vLAPS	variational Local Analysis and Prediction System
WREN_RT	Weather Running Estimate–Nowcast Realtime system
WRF	Weather Research and Forecasting
WRF-ARW	Advanced Research version of the Weather Research and Forecasting model
WRFDA	WRF Data Assimilation
WSM6	WRF single-moment 6-class microphysics parameterization
YSU	Yonsei University in Seoul, South Korea

1	DEFENSE TECHNICAL
(PDF)	INFORMATION CTR
	DTIC OCA
2	CCDC ARL
(PDF)	FCDD RLD CL
	TECH LIB
1	GOVT PRINTG OFC
(PDF)	A MALHOTRA
3	CCDC ARL
(PDF)	FCDD RLC EM
	B REEN
	H CAI
	J RABY